

1 **Spatial and morphometric analysis of a comprehensive dataset of**
2 **loess sinkholes from a small basin in the Chinese Loess Plateau**

3 Sheng Hu^{1,2}, Francisco Gutiérrez³, Fanyu Zhang⁴, Sisi Li^{1,5}, Ninglian Wang^{1,2},
4 Xi-an Li⁶, Xingang Wang⁷, Jinhui Sun¹, Songbai Wu^{1,2}

5 ¹ Shaanxi Key Laboratory of Earth Surface System and Environmental Carrying
6 Capacity, College of Urban and Environmental Sciences, Northwest University, Xi'an
7 710127, China

8 ² Institute of Earth Surface System and Hazards, Northwest University, Xi'an 710127,
9 China

10 ³ Departamento de Ciencias de la Tierra, Universidad de Zaragoza, C/ Pedro Cerbuna 12,
11 50009 Zaragoza, Spain

12 ⁴ MOE Key Laboratory of Mechanics on Disaster and Environment in Western China,
13 Department of Geological Engineering, Lanzhou University, Lanzhou 730000, China

14 ⁵ School of Information Science and Technology, Northwest University, Xi'an 710127,
15 China

16 ⁶ School of Geological Engineering and Geomatics, Chang'an University, Xi'an 710054,
17 China

18 ⁷ State Key Laboratory of Continental Dynamics, Department of Geology, Northwest
19 University, Xi'an 710069, China

20

21 **Correspondence:** Fanyu Zhang (zhangfy@lzu.edu.cn)

22

23 **Abstract.** From ~~a global perspective~~~~the perspective of the world~~, the basic mapping and
24 investigation of the loess sinkholes ~~is-are~~ far less extensive and in-depth than ~~those of karst~~
25 ~~sinkholes~~~~that of the karst sinkhole survey~~. To some extent, this ~~has limited~~~~hinders~~ people's
26 understanding of the morphological characteristics, development ~~patterns~~~~rules~~, and formation
27 mechanisms of the loess sinkholes. ~~The~~ Chinese Loess Plateau (CLP) ~~features~~~~has~~ the most
28 typical loess landforms in the world, ~~and-where~~ tens of thousands of loess sinkholes have
29 developed. However, due to the lack of high-precision and high-resolution survey data, the
30 identification, characterization, and quantification of sinkholes in the ~~CLP~~~~Loess Plateau~~ are
31 basically blank, ~~which significantly hinders in-depth research on loess sinkholes~~~~which seriously~~
32 ~~hinders the in depth study of loess sinkholes~~. ~~In this study, We-we~~ investigated a typical
33 watershed ~~on-in~~ the ~~Chinese Loess Plateau~~~~CLP~~ using photogrammetry, airborne laser scanning,
34 and ~~a~~ handheld laser scanner. Based on previous studies, this paper ~~introduces~~~~proposes~~ indices
35 and methods for the morphological quantification of loess sinkholes and constructs the first-
36 ~~ever~~ dataset of loess sinkhole morphology containing 1,194 records at the basin scale. On this
37 basis, we completed the spatial mapping of loess sinkholes, analysis of distribution patterns,
38 morphological analysis, size-frequency analysis, fitting analysis of different parameters,
39 estimation of subsurface soil erosion, in-depth investigation of typical sinkholes, and
40 quantification of the contributions of different factors to sinkhole development. These efforts
41 provide rich information for a deeper understanding of the morphological characteristics and
42 ~~genesis~~~~causes~~ of loess sinkholes and offer data support for comparative studies with sinkholes
43 in other regions. More ~~importantly~~~~critically~~, we preliminarily ~~estimate~~~~assessed~~ that the

44 subsurface soil erosion triggered by sinkholes in the study area ~~amounts to~~ reaches as high as
45 345,000 metric tons. This finding ~~underscores~~ makes it increasingly clear that loess sinkholes
46 are not only a geological disaster ~~process~~ but also a serious form of soil loss ~~a serious soil loss~~
47 ~~process~~, highlighting their undeniable significance in regional soil erosion studies and laying a
48 solid foundation for subsequent research and disaster prevention efforts. ~~Furthermore~~ Moreover,
49 we ~~suggest~~ believe that the integration of airborne laser scanning and handheld laser scanning
50 may represent a new trend in the detailed investigation of sinkholes in the future. ~~The~~ This
51 dataset is available ~~on from the~~ Zenodo platform (<https://doi.org/10.5281/zenodo.14000267>).

52 1 Introduction

53 It is widely recognized that soil erosion ~~poses~~ constitutes a global environmental problem
54 with significant ~~socioeconomic~~ societal and economic implications (Morgan, 2005; Poesen,
55 2018; Llena et al., 2024). When the term ‘soil erosion’ is ~~mentioned~~ used, most people
56 ~~envision~~ picture surface processes such as sheet, rill, gully, or gravity erosion. However,
57 subsurface mechanical erosion ~~caused by~~ related to soil piping and the ~~resulting~~ associated
58 surface collapse ~~remains largely~~ is widely overlooked (Bernatek-Jakiel and Poesen, 2018). The
59 ~~extensive~~ vast international literature on soil erosion reveals a pronounced knowledge gap in an
60 ~~evident knowledge gap regarding~~ soil piping research. Soil piping ~~involves~~ refers to the
61 formation of shallow conduits in soils and weakly consolidated sediments ~~through~~ by seepage,
62 pipe flow, and mass movements (e.g., wall and roof collapse) (Bernatek-Jakiel and Poesen,
63 2018). Soil pipes, ~~owing to their concealed~~ due to their hidden nature and complex patterns, are
64 typically detected only ~~after~~ once their collapse reaches the surface, ~~forming~~ to form a

65 sinkhole (Donnelly, 2008; Bernatek, 2015; Bernatek-Jakiel et al., 2017). Ground instability
66 ~~resulting from associated with~~ sinkhole development poses threats to agriculture, transportation
67 infrastructure, water storage facilities, oil and gas pipelines, buildings, and other human assets
68 and activities (Gibbs, 1945; Gutiérrez et al., 2003, 2014; Richards and Reddy, 2007; Peng et al.,
69 2018; Hu et al., 2020). Piping sinkholes ~~contribute to cause~~ soil erosion and can ~~trigger or~~
70 ~~exacerbate induce or favor~~ hazardous processes such as ground collapse, landsliding, debris
71 flows, ~~or and~~ gullyng (Peng et al., 2018; Li et al., 2020; Hu et al., 2022; Wang et al., 2024).
72 Therefore, gaining insight into the factors controlling piping-related sinkholes, their
73 morphometry, and spatial distribution patterns is of ~~paramount prime~~ scientific and practical
74 importance (Hofierka et al., 2018; Bernatek-Jakiel et al., 2019).

75 The identification of sinkholes and the ~~production of comprehensive sinkhole inventories~~
76 ~~are a fundamental and challenging task~~ compilation of comprehensive sinkhole inventories
77 constitute a fundamental yet challenging task. In recent decades, several countries have conducted
78 extensive research on karst and piping sinkholes and developed national or regional
79 geodatabases (Gao et al., 2002, 2005; Farrant and Cooper, 2008; Rajabi, 2018; Vennari and
80 Parise, 2022; Hu et al., 2024). Traditional sinkhole mapping primarily relies on topographic
81 maps, digital elevation models (DEM), historical aerial photography, or satellite imagery
82 (Panno et al., 1997; Panno and Luman, 2013; De Carvalho Júnior et al., 2014; Vajedian and
83 Motagh, 2019; Gökkaya et al., 2021). However, ~~the data collected~~ the data acquired through
84 conventional methods are often hampered by poor spatial resolution, making them inadequate
85 for the comprehensive and accurate mapping and morphometric characterization of soil

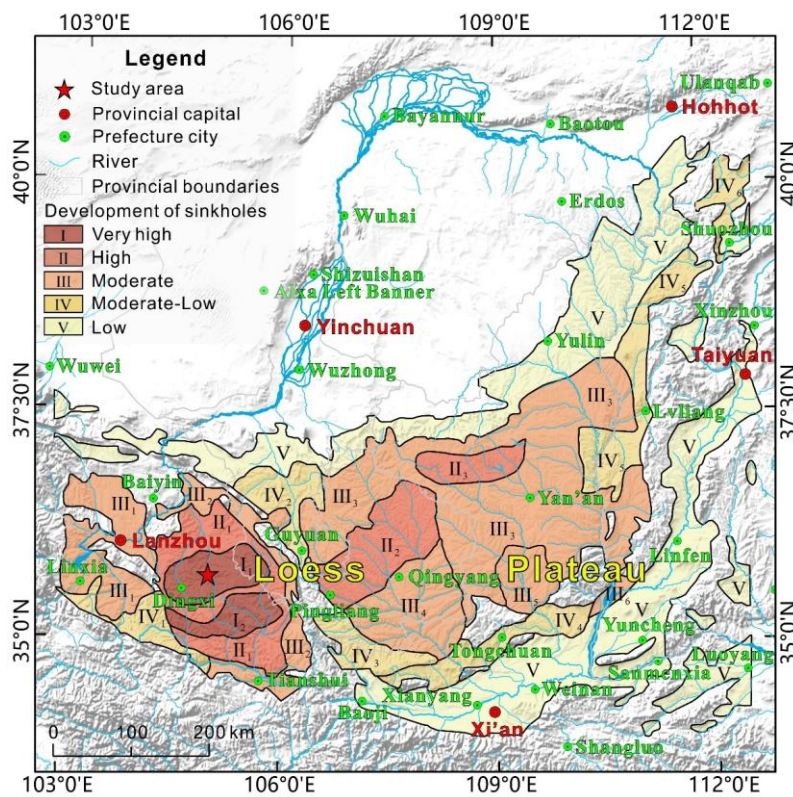
86 sinkholes, which are usually small. Consequently, researchers have increasingly turned to
87 ~~started to use~~ unmanned aircraft systems (UAS) equipped with optical lenses, LiDAR sensors,
88 and thermal cameras to investigate piping sinkholes (Lee et al., 2016; Wu et al., 2016; Hofierka
89 et al., 2018; Hu et al., 2020; Li et al., 2024). UAS technology can capture imagery and
90 topographic data with high resolution and accuracy, and may even allow for vegetation
91 ~~filtering~~filtering-vegetation in the case of LiDAR data. Despite the variety of techniques and
92 approaches currently available, each still ~~possesses~~carries inherent limitations or shortcomings
93 (Bernatek-Jakiel and Poesen, 2018). For instance, although UAS-based photogrammetry can
94 yield high-resolution topographic models, those models do not allow ~~for the reliable~~the reliable
95 measurement of 3D morphometric parameters of piping sinkholes, such as depth or volume (Li
96 et al., 2024). Airborne LiDAR, while capable of partly penetrating vegetation to reveal the
97 underlying ground surface, typically employs orthogonal scanning, ~~thereby missing~~missing
98 zones along the vertical walls of collapsed pipes, and ~~consequently failing~~thus failing to capture
99 the complete inner morphology of the sinkholes (Jiang et al., 2024). The aforementioned
100 mapping technologies and methods are suitable for regional sinkhole surveys, but they are
101 ~~inadequate for~~are not suitable for characterizing the internal morphology of individual
102 sinkholes. In recent years, handheld laser scanners based on simultaneous localization and
103 mapping (SLAM) technology have been developed and successfully applied to forest surveys,
104 archaeological studies, as well as tunnel, ~~—~~ and sinkhole investigations (Jones and Beck, 2017;
105 Konsolaki et al., 2020; Mokroš et al., 2021; Yuan et al., 2022; Hu et al., 2024; Jiang et al., 2024).
106 When conducting non-destructive identification and characterization of soil pipes and their

107 ~~associated the associated~~ sinkholes, it is essential to select the most suitable investigation
108 technique or to combine several complementary methods, ~~taking into account considering~~
109 factors such as the characteristics of the target features and the survey area (Bernatek-Jakiel and
110 Kondracka, 2016; Borah et al., 2022).

111 A ~~recent~~ review on soil piping (Bernatek-Jakiel and Poesen, 2018) ~~synthesizes current~~
112 ~~knowledge globally and outlines directions for future research~~ ~~provides a global synthesis of~~
113 ~~current knowledge and delineates directions for future research~~. By collating data from 230
114 documented piping sites worldwide, the authors produced the first global map of soil-piping
115 investigations, demonstrating that piping erosion occurs across all climate zones and most soil
116 types. ~~However, Regrettably,~~ the review reveals a striking paucity of research on soil pipes in
117 the Chinese Loess Plateau (CLP), with only two documented study sites. It is widely recognized
118 that the CLP, covering 64×10^4 km², hosts the world's most representative loess accumulation.

119 Due to the relatively high permeability, collapsibility, and ~~water sensitivity wetness~~ of loess
120 deposits, together with ~~their porous and jointed structure~~ ~~its porous and jointed structure~~, pipes
121 and sinkholes can ~~readily~~ ~~easily~~ form under the presence of water (Li et al., 2010; Geng et al.,
122 2023). In recent years, some scholars in China have ~~recognized~~ ~~identified~~ loess sinkholes as a
123 specific geological hazard and have called for increased ~~attention~~ ~~focus~~ and research on this
124 process ~~given its growing economic implications~~ ~~with growing economic implications~~ (Li et al.,
125 2010, 2020; Peng et al., 2018). The intensity map of sinkhole development in the ~~Chinese Loess~~
126 ~~Plateau~~ ~~CLP~~ (Fig. 1) ~~shows~~ ~~indicates~~ that the ~~western~~ ~~west~~ region exhibits a higher intensity of
127 sinkhole development compared to the east, particularly in the Dingxi and Huining areas, where

128 sinkhole densities typically reach 243 and 265 sinkholes per km², respectively (polygon I₁ in
 129 Figure 1) (Peng et al., 2018; Hu et al., 2020). Notably, no regional morphometric datasets of
 130 piping sinkholes have yet been published, constraining/limiting our understanding of their
 131 morphological characteristics and developmental patterns.



132
 133 **Figure 1.** Map illustrating/showing the degree of piping-related sinkhole development in the
 134 Chinese Loess Plateau, grouped/classified into five categories (Peng et al., 2018; Hu et al.,
 135 2020). The star denotes/indicates the location of the study area within a zone of very
 136 high/within a region with very high degree of sinkhole development.

137 In view of the above, the principal objectives of this study include/are:

138 (4i) to ~~perform~~~~conduct~~ a comprehensive and high-resolution survey of loess sinkholes in
139 a representative basin of the CLP by integrating UAS photogrammetry, airborne LiDAR, and a
140 SLAM-based handheld laser scanner (HLS);

141 (2ii) to characterize the morphometric features of the sinkholes and produce an open-
142 access database comprising 1194 sinkhole records, ~~supplemented~~~~complemented~~ with data on
143 multiple attributes;

144 (3iii) to analyze the spatial distribution patterns of the sinkholes and their relationships
145 with other landforms in order to gain insight into the main controlling factors;

146 (4iv) to ~~conduct~~~~carry-out~~ an in-situ investigation inside a typical sinkhole using the HLS,
147 evaluating the potential and advantages of SLAM technology for ~~complete~~ ~~full~~-sinkhole
148 characterization.

149 Through these efforts, we aim to partially fill the current knowledge gap on loess sinkholes
150 in the CLP and identify suitable surveying approaches. ~~This will make available a unique case-~~
151 ~~study dataset to the global soil-piping community and will provide a scientific basis for~~
152 ~~assessing and managing sinkhole risk in the region.~~~~This will make available to the global soil-~~
153 ~~piping community with a unique case study dataset and will provide a scientific basis for~~
154 ~~assessing and managing sinkhole risk in the region.~~ The presented results reveal the strikingly
155 large subsurface erosion volume attributable to piping erosion, underscoring that soil-piping
156 research merits intensified attention, rather than continued neglect.

157 2 Study area

158 The study area is a small leaf-shaped watershed drained by the N-flowing Sunjiacha stream.

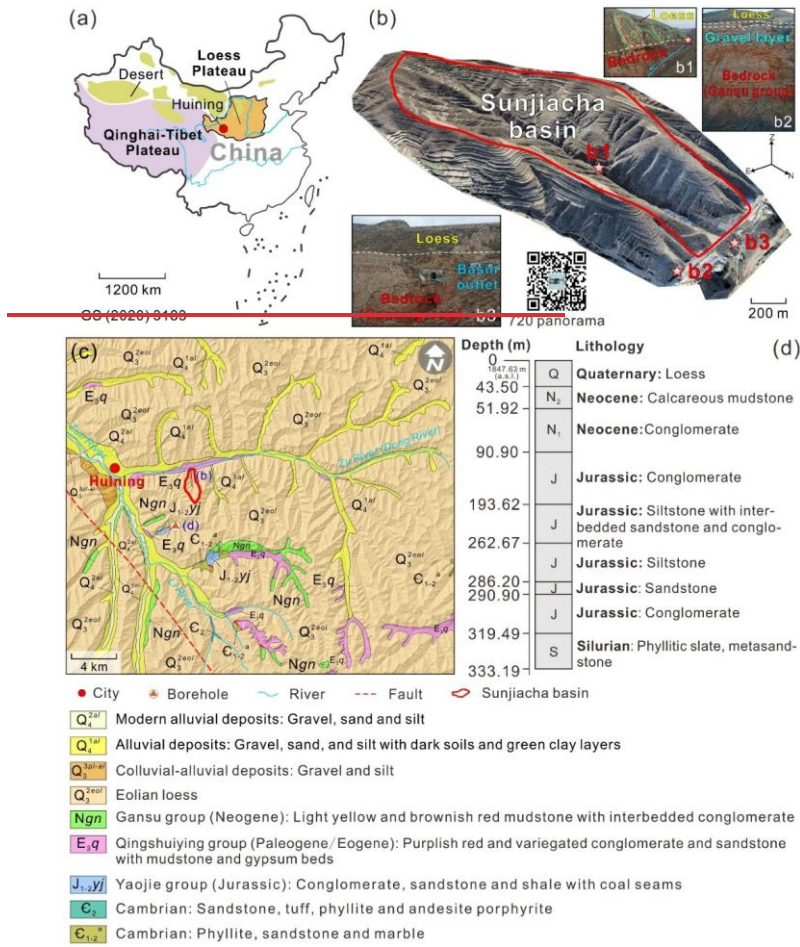
159 It is located in the southwestern sector of the Loess Plateau of China, approximately 5 km east
160 of Huining city (Figs. 2a-c). The drainage basin is approximately 2960 m long, and 1280 m
161 wide, ~~covering~~ about 2.4 km², and ~~is characterized by displays~~ sparse grassland
162 vegetation. The elevation ranges from 2070 m a.s.l. (highest point of the divide) to 1724 m a.s.l.
163 (outlet), ~~resulting in yielding~~ a local relief of 346 m. The region is characterized by a semi-arid
164 temperate monsoon climate, with a mean annual precipitation of 370 mm. ~~Much of the Great~~
165 ~~part of the~~ rainfall occurs between May and September, and frequent severe rainfall events can
166 account for up to 96% of the monthly precipitation (Hu et al., 2020). Sunjiacha stream is an
167 ephemeral channel that carries water flow after storms or rainy periods. ~~Most of Great part of~~
168 the slopes in the basin, with the exception of some sectors in the lower part, have been
169 transformed into a terraced landscape on loess deposits for cultivation and ~~erosion control to~~
170 ~~prevent soil erosion~~ (Fig. 2b).

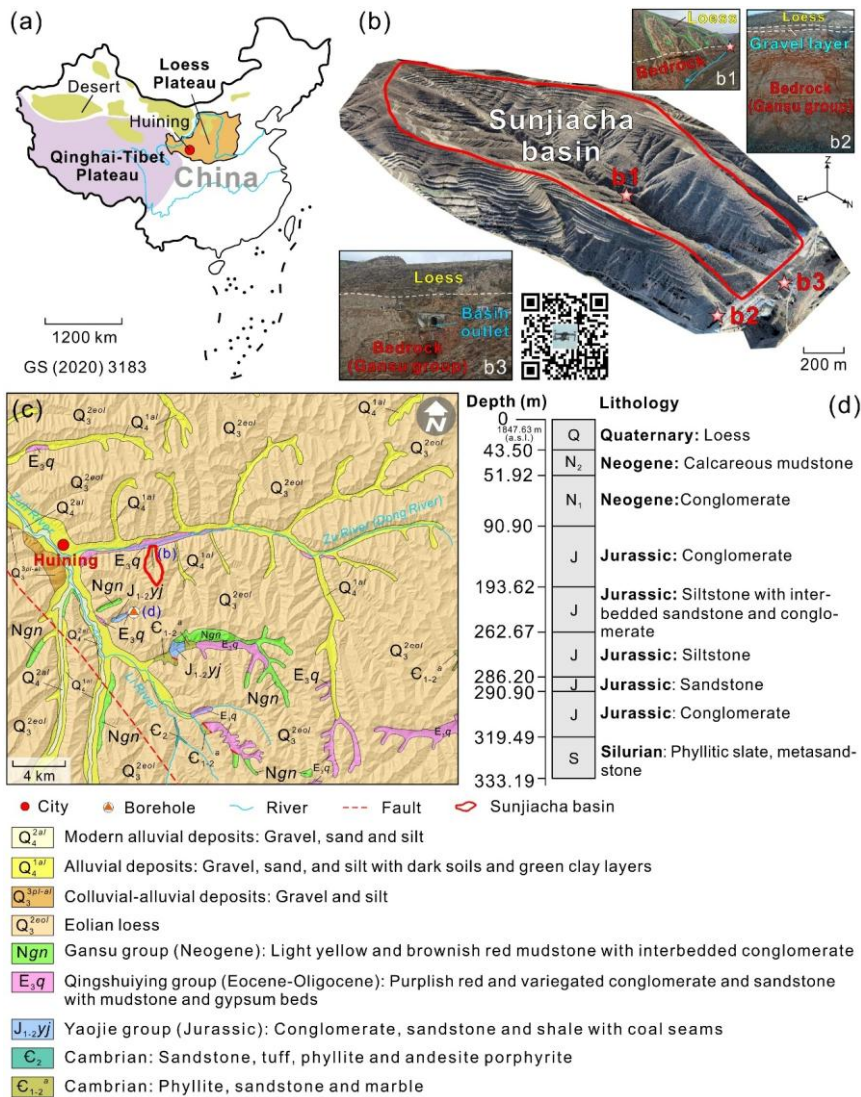
171 ~~From From the a~~ geological perspective, the investigated zone is located in the Longxi
172 Basin. Its development began during the Yanshan orogeny (ca. 205–66 Ma),
173 ~~continued expanded~~ further during the Himalayan orogeny (ca. 50 Ma to present), and finally
174 took shape as the Longxi graben basin by the late Neogene. The basement of the basin is
175 composed of Proterozoic metamorphic rocks, Paleozoic volcano-sedimentary rocks,
176 Caledonian intrusive rocks and Mesozoic-Cenozoic sedimentary successions. Since the end of
177 Neogene to ~~the~~ Quaternary, the Longxi Basin has been uplifted ~~together with along with~~ the
178 Qinghai-Tibet Plateau and its surrounding mountains (Niu, 2023). The tectonic uplift in the
179 Quaternary has been accompanied by (Figs. 2b, c): (1) downcutting of the drainage network

180 into the Neogene sediments of the Gansu group; and (2) accumulation of loess and terraces over
181 the relatively flat Gansu group red beds, forming a thick loess-paleosol succession. The
182 1:200,000 scale regional geological map indicates that most slopes in the area are underlain by
183 the Q₃ aeolian loess (Malan loess), while Q₄ alluvial and colluvial deposits, largely derived
184 from the former, ~~are mainly found~~~~primarily occur~~ in the valley floors (Fig. 2c). Fig. 2d shows
185 a simplified log of the 333 m deep Huining #11 borehole drilled 2.6 km ~~south of S~~~~of~~ the
186 Sunjiacha basin by the China Geological Survey in 1972, ~~revealing~~~~indicating~~ a Quaternary
187 loess ~~thickness of 43.5 m~~~~43.5 m thick~~. In the 1960s, Liu (1964, 1965) observed a gradual NW-
188 to-SE grain-size decrease in the loess ~~across~~~~in~~ the ~~Loess Plateau~~~~CLP~~, and divided it into three
189 zones: sand loess, typical loess, and clayey loess. This spatial pattern is attributed to factors
190 such as the distance from the source area and the southeastward weakening of winds in winter
191 (Yang and Ding, 2017). Previous studies have shown that the Huining loess ~~contains~~~~has~~ both
192 dust from inland desert areas and detritus generated during the Pleistocene glaciations on the
193 Qinghai-Tibet Plateau (Peng, 2014). Because Huining is close to both source regions, relatively
194 coarse sand and silt particles were deposited here by the northwesterly winds. Thus, the large
195 pore size characteristic of the Q₃ Malan loess is particularly pronounced in this area. The Q₃
196 Malan loess is a light grey-yellow silt-dominated deposit with relatively uniform particle
197 distribution, loose granular texture and blocky morphology. The grain size of the loess-paleosol
198 sequence at Duanxian site (S0~L29; 62 km north of our study area) studied by Niu (2023) is
199 generally coarse, with a median particle size ranging from 12 to 38.8 μm (silt size range: 2~50
200 μm). Particles >32 μm and >63 μm represent around 60% and 25% of the silt-dominated deposit,

201 respectively (Niu, 2023).

202 The thickness of the Q₃ Malan loess is highly variable, ranging from several meters to tens
203 of meters. Under the presence of infiltration water, the Q₃ Malan loess, which is often affected
204 by vertical joints~~commonly affected by vertical joints~~, is highly susceptible to hydrocompaction
205 and piping, giving rise to~~leading to the formation of~~ unique loess sinkhole landscapes. In fact,
206 this area is widely recognized as having the highest density of loess sinkholes in the vast Loess
207 Plateau, covering 6370 km² (2.33% of the loess accumulation in China) (Fig. 1). The aAverage
208 density of sinkholes in our study area is ca. 500498 sinkholes/km². The investigated drainage
209 basin, characterized by a dendritic gully network and terraced slopes, displays a large number
210 of loess-related ground instability features, including 1194 loess collapse sinkholes and 288
211 landslides (Fig. 3). The latter include slope movements with deep and shallow sliding surfaces,
212 typically induced by fluvial undercutting, artificial excavations, and intense~~severe~~ rainfall
213 events.

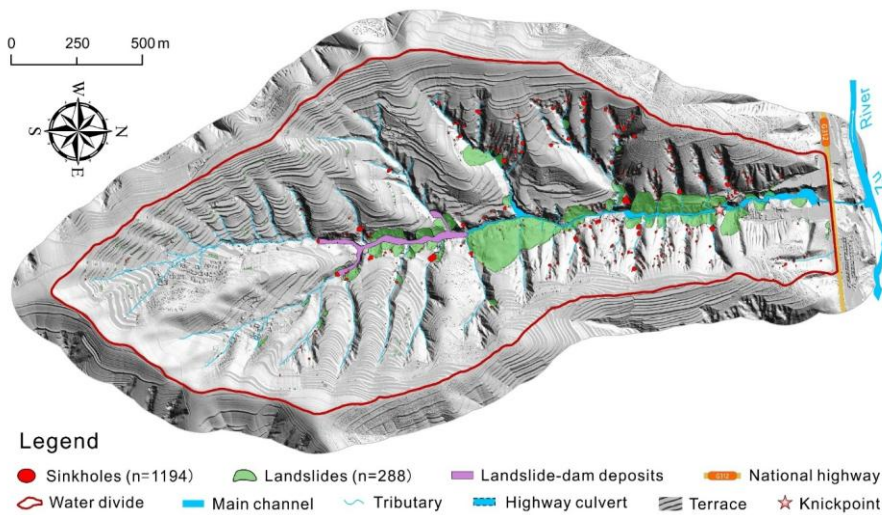




215
 216 **Figure 2.** Geographic and geological setting of the Sunjiacha drainage basin within the Loess
 217 Plateau: (a) Location of the study area in the SW Loess Plateau in China; (b) 3D
 218 model of the Sunjiacha basin generated by Structure from Motion Photogrammetry with UAS
 219 images. The QR code provides access (<https://www.720yun.com/t/0cvktq7yg2w>) to an

域代码已更改

220 online panorama of the study area ~~created~~^{generated} with drone images; (c) 1:200,000 scale
221 regional geological map (data source: [available at http://dcc.ngac.org.cn/](http://dcc.ngac.org.cn/)); (d) Stratigraphic
222 log of the Huining #11 borehole drilled for coal exploration 2.6 km south of the study area
223 (see location in **c**) (data source: [available at http://zk.cgsi.cn/](http://zk.cgsi.cn/)).



224

225

226

227

228

229

230

231

232

233

234

235

236

237

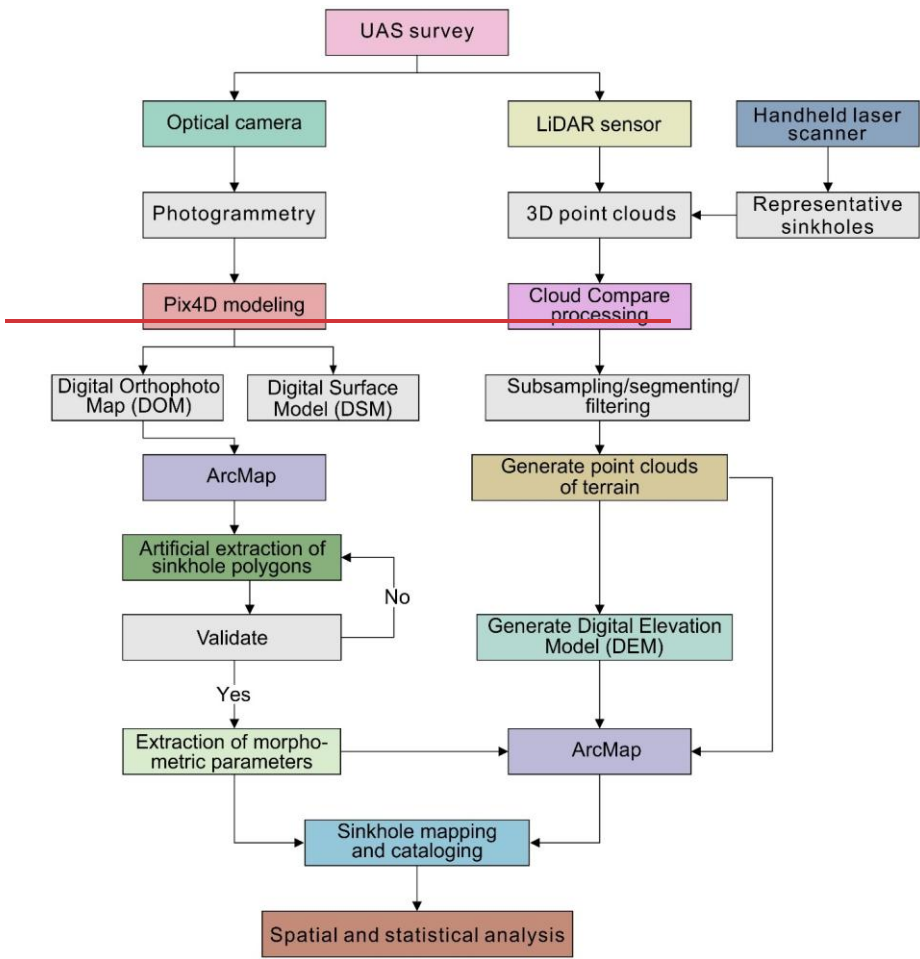
Figure 3. Geomorphological map illustrating showing the distribution of loess sinkholes, landslides, and deposits accumulated upstream of a landslide dam in the Sunjiacha basin.

3 Methods

3.1 Technical procedure

The flow diagram in Figure 4 outlines the data acquisition and analysis approach adopted followed in this investigation, which consisted of several key steps comprising several steps. Initially, we performed surveye conducted surveys using an unmanned aircraft system (UAS) equipped with optical cameras and LiDAR sensors, along with as well as utilizing a handheld laser scanner (HLS). Subsequently, the data collected during these surveys enabled the generation in the surveys allowed the generation of a Digital Orthophoto Map (DOM), a bare-surface Digital Surface Model (DSM), a Digital Elevation Model (DEM), and 3D terrain point clouds. The drone imagery was processed using with the Structure from Motion Photogrammetry photogrammetry software Pix4D Mapper v4.5.6 (<https://www.pix4d.com/>),

238 while the open-source Cloud Compare v2.13-2 software (<http://www.cloudcompare.org/>) ~~was~~
239 ~~used to analyze~~~~was utilized for analyzing~~ the point clouds. ArcMap 10.5 was used to manually
240 map the sinkholes and extract planimetric and three-dimensional morphometric parameters
241 ~~from by using~~ the DOM, DEM and relief maps. This ~~enabled the creation of~~ ~~allowed the~~
242 ~~construction of~~ a cartographic sinkhole inventory ~~containing~~~~including~~ a number of categorical
243 and numerical attributes for the morphometric and statistical analysis of the sinkholes. 3D data
244 of the loess sinkholes, ~~such as elevation and depth, were derived from~~ ~~such as elevation and~~
245 ~~depth were extracted from~~ noise-filtered terrain point clouds acquired with airborne LiDAR,
246 rather than directly from the UAS-derived DSM, ~~which significantly enhanced~~ ~~significantly~~
247 ~~enhancing~~ the accuracy of the parameters.



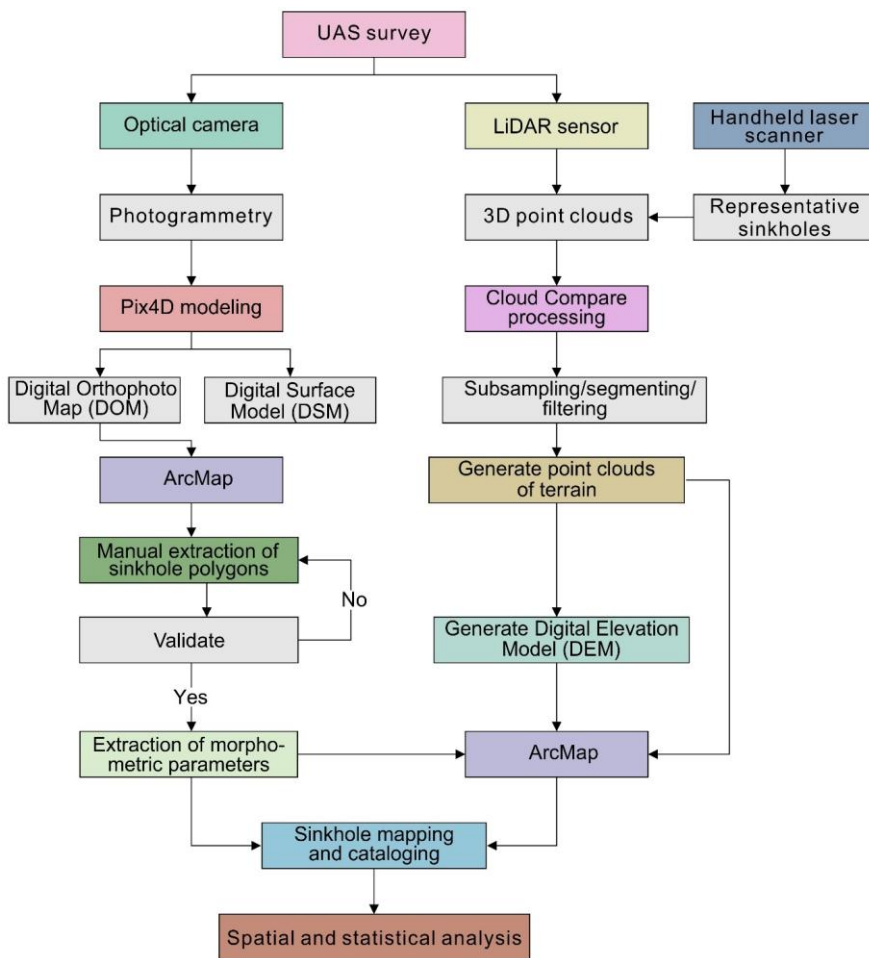


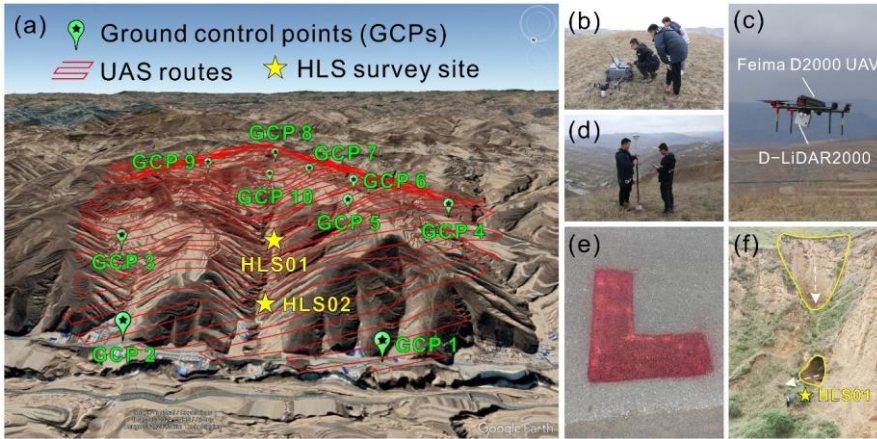
Figure 4. Flow chart ~~outlining~~ ~~illustrating~~ the data collection, processing, and analysis approaches ~~used in this study.~~

3.2 Field investigations

3.2.1 UAS survey

On April 9, 2021, we engaged the professional company Feima Robotics to conduct a detailed survey of the research area using a D2000 UAS (Figs. 5a-e). We ~~carried out~~ ~~executed~~

256 two flight missions at a height of 200 m utilizing the D-Lidar 2000 LiDAR sensor (linear
257 scanning) and the D-CAM2000 optical camera mounted on the drone. Images were taken with
258 longitudinal and lateral overlaps of 70% and 60%, respectively. Point clouds were acquired
259 ~~with taken with a~~ lateral overlap of 40%. A total of 11 ground control points (GCPs) were
260 distributed across the area and measured with a DGPS. Detailed specifications of the UAS and
261 its sensors are available at <http://www.feimarobotics.com/zhen/productDetailD2000>. The D-
262 Lidar 2000 module employs three-echo technology, which ensures effective penetration
263 through vegetation to obtain more accurate bare-ground data~~ensuring effective penetration~~
264 ~~through vegetation to obtain more accurate bare ground data~~. After completing the field survey,
265 we pre-processed the collected data with the UAV Manager v1.7.0 software to produce a 3 cm
266 resolution Digital Orthophoto Map (DOM) and a Digital Surface Model (DSM), along with raw
267 point cloud data (40 GB; average density of 192 points/m²). The modeling report from UAV
268 Manager indicated that the average RMSE (root-mean-square error) for the 11 ground control
269 points (GCPs) was 0.0137 m, with RMSEs of 0.012 m, 0.014 m_x and 0.015 m for the X, Y_x and
270 Z coordinates, respectively. An elevation accuracy assessment of 19 laser point cloud validation
271 points measured with the DGPS revealed an average RMSE of 0.029 m, with a maximum error
272 of 0.058 m.



273
 274 **Figure 5.** Surveying of the study area with an UAS (Li et al., 2024) and a handheld laser
 275 scanner: (a) Terrain model of the study area draped by a Google Earth image. Red lines depict
 276 the UAS flight paths indicate the route of the UAS. Green paddle icons show the distribution
 277 of ground control points (GCPs) used to improve the accuracy of the UAS models. Yellow
 278 stars indicate the location of the handheld laser scanner surveys. (b-e) Unmanned aerial
 279 system field operations with the control unit (eb) and the drone (dc), combined with a DGPS
 280 (d) and GCPs (e) measured with a DGPS (d); (f) Using the GeoSLAM (ZEB Horizon)
 281 handheld laser scanner to scan the interior of a sinkhole in a steep slope with an opening at the
 282 bottom.

283 **3.2.2 Handheld laser scanner survey**

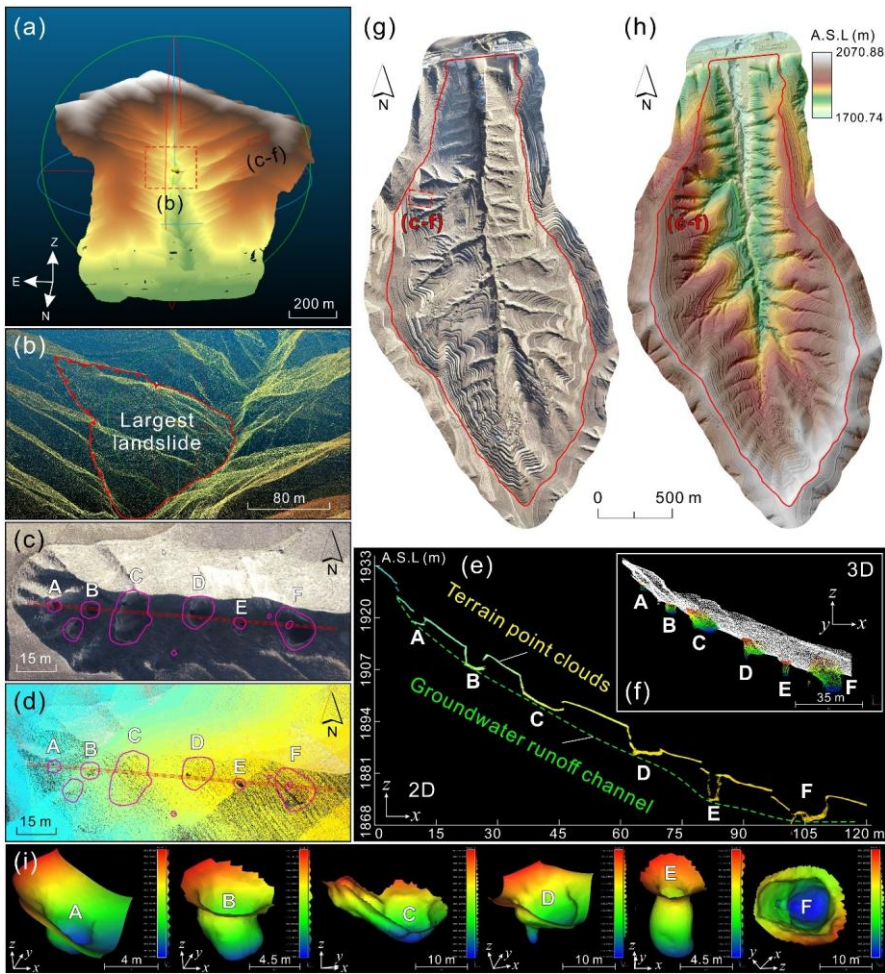
284 We used a GeoSLAM ZEB Horizon handheld LiDAR scanner (<https://geoslam.com/>) with
 285 a maximum range of 100 m to carry out high-resolution scans of thirteen representative
 286 sinkholes (1 sinkhole in-at HLS01 site; 12 sinkholes in-at HLS02 site; see location in Figures
 287 5a, f). This device utilizes SLAM (Simultaneous Localization and Mapping) technology,
 288 enabling real-time recording of point cloud data of the terrain or objects with accurate
 289 geographic coordinates. which can record point cloud data of the terrain or objects in real time

290 ~~obtaining accurate geographic coordinates.~~ It weighs 1.45 kg, and records 300,000 points per
291 second with a measurement error ~~ranging from~~ 6 mm to 30 ~~mm~~. After the field survey, we
292 pre-processed and post-processed the point cloud data using GeoSLAM Draw [v4.0](#) and Cloud
293 Compare software [v2.13.2](#), and subsequently we obtained noise-filtered terrain point clouds
294 and DEMs of the representative sinkholes.

295 **3.2.3 Surveying and mapping**

296 ~~Figure 6 shows~~ illustrates some of the products derived from the UAS survey. We filtered
297 the raw point clouds using the Cloth Simulation Filter (CSF) developed by [Zhang et al. \(2016\)](#)
298 in Cloud Compare [v2.13.2](#). The main parameter settings were: General parameter setting –
299 check Steep slope and Slope processing options; Advanced parameter setting – Cloth resolution
300 0.5 m, Maximum iterations 999, Classification threshold 0.1 m. [Figure 6a](#) shows the terrain
301 point cloud processed in Cloud Compare [v2.13.2](#) with above-surface noise ~~removed~~ filtered out
302 (~~e.g., buildings, people, vehicles, vegetation, towers, and power lines~~ buildings, people, vehicles,
303 ~~vegetation, towers, and power lines~~). [Figures 6b-f](#) show enlarged views of the dashed boxes
304 indicated in [Figures 6a, g-h](#). [Figure 6b](#) illustrates the largest landslide ~~of~~ in the study area.
305 [Figures 6c](#) and [6d](#) depict an orthoimage and a terrain point cloud of a gully with a string of
306 sinkholes related to a subsurface conduit created by internal erosion. [Figures 6e](#) and [6f](#) display
307 the 2D profile of the terrain point cloud and an excerpt of the 3D point cloud of a gully with
308 numerous sinkholes, respectively. [Figure 6g](#) shows the 6.87 cm resolution Digital Orthophoto
309 Map (DOM) derived from the drone images. [Figure 6h](#) presents the 0.5 m resolution Digital
310 Elevation Model (DEM) generated from the terrain point cloud data in [Figure 6a](#). [Figure 6i](#)

311 depicts the 3D models generated by Poisson Surface Reconstruction in Cloud Compare [v2.13.2](#),
 312 based on LiDAR point-cloud data from six sinkholes. These spatial data provide the basis for
 313 mapping and cataloging sinkholes, identifying sediment-discharge holes, and extracting
 314 morphometric parameters.



315 **Figure 6. Results of the UAS survey**
 316 **UAS survey results:** (a) Bare-surface point cloud of the
 317 study area after filtering out above-surface objects; (b-f) Enlarged views of the areas indicated

318 ~~by dashed boxes in~~ Partial enlargements of (a); (b), ~~The L~~ largest landslide ~~of in~~ the study area;
319 (c-e) Orthoimage, point cloud, and a point-cloud section of a row of loess sinkholes (purple
320 line in d) ~~within~~ a collapsed gully, respectively; (f) ~~3D perspective view of the area shown in~~
321 ~~3D perspective of (d)~~; (g) Digital orthophoto map (DOM) generated from images ~~acquired~~
322 ~~during~~ captured by the UAS survey; (h) Digital elevation model (DEM) ~~derived from~~
323 ~~the generated from~~ bare-surface point clouds; (i) Poisson surface reconstruction of sinkholes
324 A-F ~~as seen in~~ ~~in~~ ~~of~~.

设置了格式: 字体颜色: 自动设置

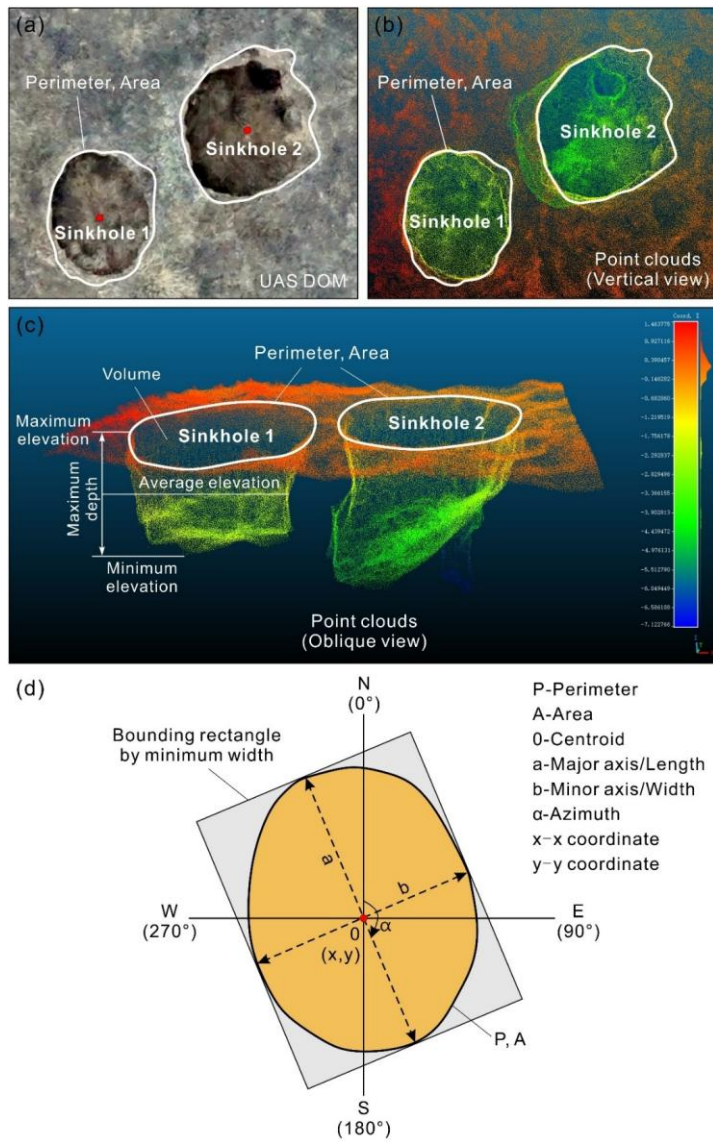
325 3.3 Basic morphometric parameters and extraction methods

326 ~~Drawing on~~ Based on a literature review on studies about loess sinkholes and karst dolines
327 worldwide, we selected a number of morphometric parameters for the geometrical
328 characterization of the loess sinkholes (e.g., Day, 1983; Liu and Wang, 2008; De Waele and
329 Gutiérrez, 2022 and references therein). Table 1 presents the selected ~~some~~ parameters, their
330 definitions, and the approach used for their automatic computation. ~~The key morphological~~
331 ~~parameters and their definitions~~ Key morphological parameters and their interpretations are
332 illustrated in Figure 7.

333 **Table 1** Morphometric parameters used for the characterization of loess sinkholes: Index,
 334 definition and computing method ~~computing method of morphology of loess sinkholes.~~

Parameter	Unit	Computing method	Explanation	Reference
Coordinates	°	Calculate geometry in ArcMap attribute table	X, Y coordinates of the centroid of the sinkhole polygon	
Length (<i>L</i>)	m	Length of the fitted minimum bounding rectangle	Length of the major axis, given by the planimetric distance between the antipodal points of the perimeter	Kobal et al, 2015; Wu et al, 2016
Width (<i>W</i>)	m	Width of the fitted minimum bounding rectangle	Width perpendicular to major axis, given by the width of the fitted minimum bounding rectangle	Kobal et al, 2015; Wu et al, 2016
Azimuth (<i>Azi</i>)	°	ArcMap Minimum Bounding Geometry tool	Clockwise angle between the North and the major axis	Bruno et al, 2008; Kobal et al, 2015; Öztürk et al, 2018
Maximum elevation (<i>E_{max}</i>)	m	Extracted from point cloud data using LAS Point Statistics by Area tool in ArcMap	Maximum elevation of the sinkhole perimeter	
Minimum elevation (<i>E_{min}</i>)	m		Minimum elevation at the sinkhole bottom	
Average elevation (<i>E_{ave}</i>)	m		Average elevation of the 3D points that define the sinkhole depression	
Maximum depth (<i>D_{max}</i>)	m	Extracted from point cloud data	Maximum elevation minus minimum elevation	De Waele and Gutiérrez, 2022; Sevil and Gutiérrez, 2023
Perimeter (<i>P</i>)	m	Calculate geometry in ArcMap attribute table	Planimetric length of the mapped edge of the sinkhole	Liu and Wang, 2008
Area (<i>A</i>)	m ²	Calculate geometry in ArcMap attribute table	Planimetric area enclosed by the perimeter	Liu and Wang, 2008
Volume (<i>V</i>)	m ³	$V=A \times D_{max}$	Volume of the 3D space corresponding to the sinkhole depression	Gökkaya et al., 2021; De Waele and Gutiérrez,

			2022
Elongation ratio (<i>ER</i>)	$ER=L/W$ or $ER=a/b$, where <i>L</i> (or <i>a</i>) and <i>W</i> (or <i>b</i>) are the major and minor axes (length and width) of the sinkhole, respectively	Length to width ratio	Day, 1983; Basso et al., 2013; Zumpano et al., 2019
Circularity index (<i>CLI</i>)	$CLI = 4\pi A/P^2$	Ratio between the area of the sinkhole and the area of a theoretical sinkhole having a circumference equal to the perimeter of the actual sinkhole. The lower the value below 1, the further to a perfect circular shape	De Carvalho Júnior et al., 2014
Compactness index (<i>COI</i>)	$COI = A/A_c$, where <i>A_c</i> is the area of the smallest circle circumscribing the sinkhole perimeter	Quantifies how much the shape of the sinkhole perimeter is close to a circle. The lower the value below 1, the more complex the sinkhole perimeter	Cole, 1964; Kim and Anderson, 1984; Li et al., 2013; Zhu and Pierskalla, 2016
Length to Depth ratio (<i>LDr</i>)	$LDr=L/D_{max}$	Ratio between sinkhole length and depth	Day, 1983



336
 337 **Figure 7.** Diagrams illustrating showing the key morphometric parameters of the loess
 338 sinkholes: (a) Orthoimage Images of sinkholes; (b) Vertical view of Psinkholes point clouds
 339 oint clouds of sinkholes (located at HLS 02 in Figure 5a) in vertical view; (c) Oblique view of
 340 Point clouds of sinkholes point clouds in oblique view; (d) Schematic diagram Diagram of key

341 morphometric parameters of sinkholes.

342 **4 Results**

343 **4.1 Sinkhole mapping and inventorying**

344 Given the ~~exceptionally~~^{utmost} high-resolution of the data used for mapping, the inventory
345 can be considered ~~nearly complete~~^{as complete}, even including small decimeter-scale holes.
346 This information furnished a database of 1194 loess sinkholes in the study area, ~~each~~
347 ~~characterized by including~~ multiple attributes (**Table 1** and **Data availability**): topographic
348 (coordinates, azimuth, maximum, minimum and average elevation); morphometric (length,
349 width, depth, perimeter, area, volume, geometrical indexes); and geomorphic (soil loss). The
350 inventory also differentiates 1162 single sinkholes, and 32 compound sinkholes resulting from
351 the aggregation of two or more adjacent sinkholes. This ~~comprehensive~~^{complete} database
352 serves as the basis for the morphometric-statistical analysis presented in this work. For the
353 detailed cataloging and the statistical parameters of these sinkholes, please refer to **Table 2** and
354 **Data availability**. Additionally, 9 thematic maps were generated with some parameters (length,
355 maximum depth, perimeter, area, volume, elongation ratio, circularity index, compactness
356 index, length to depth ratio) to explore spatial patterns of different value ranges. **Table 2** presents
357 the main statistics of the sinkholes ~~grouped~~^{separated} into three categories: all, single, and
358 compound.

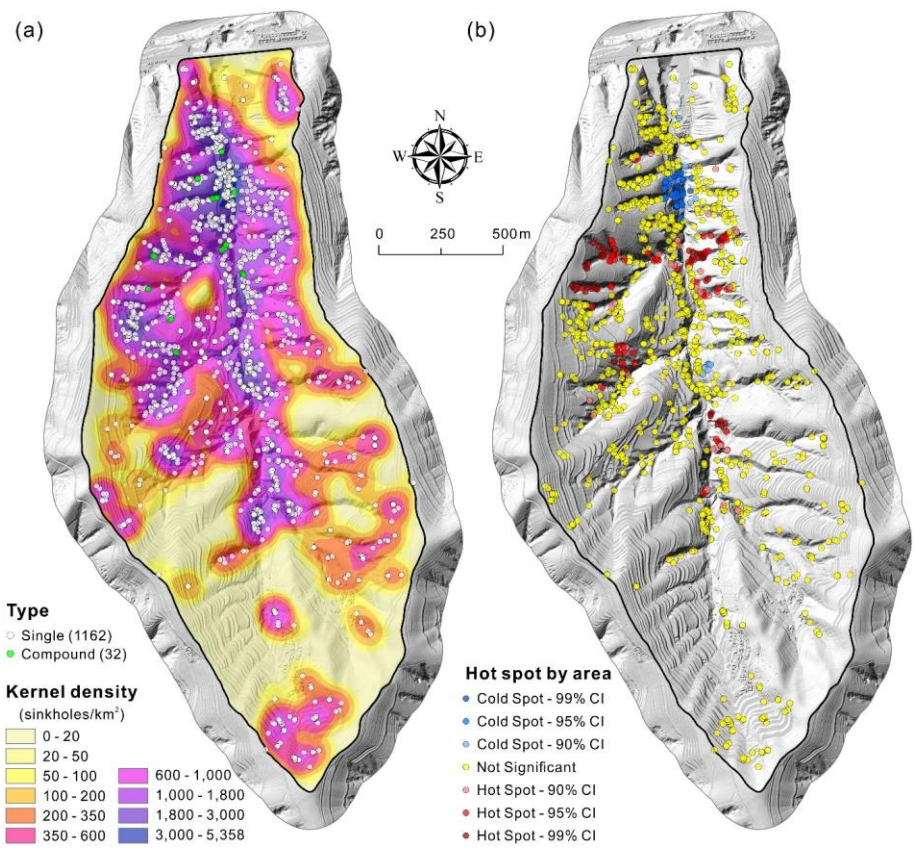
359 **Table 2** Summary statistics of morphometric parameters for different types of sinkholes. ~~Main~~
 360 ~~statistics of different types of sinkholes.~~

Statistical indicators	All sinkholes (1194)	Single sinkholes (1162)	Compound sinkholes (32)
Length (m)			
Range	0.19–35.11	0.19–35.11	0.88–33.9
Mean	3.75	3.65	7.37
Median	2.28	2.26	3.69
Depth (m)			
Range	0.42–29.60	0.42–29.60	2.05–18.50
Mean	6.55	6.48	8.36
Median	5.30	5.214	7.76
Perimeter (m)			
Range	0.60–104.14	0.60–98.92	2.67–104.14
Mean	10.75	10.45	21.51
Median	6.43	6.40	10.47
Area (m²)			
Range	0.03–662.18	0.03–662.18	0.50–635.75
Mean	17.75	16.42	66.19
Median	2.94	2.93	7.97
Volume (m³)			
Range	0.21–19601.27	0.21–19601.27	2.66–8405.93
Mean	334.75	310.79	1002.98
Median	42.78	42.10	81.28
Elongation ratio			
Range	1–4.55	1–4.55	1.04–1.98
Mean	1.37	1.37	1.31
Median	1.30	1.30	1.28
Circularity index			
Range	0.33–0.98	0.33–0.98	0.74–0.96
Mean	0.89	0.89	0.88
Median	0.92	0.92	0.90
Compactness index			
Range	0.45–0.88	0.45–0.88	0.70–0.82
Mean	0.78	0.78	0.77
Median	0.78	0.78	0.76
Length to depth ratio			
Range	0.11–6.06	0.11–6.06	0.30–2.56
Mean	0.84	0.87	0.87
Median	0.77	0.77	0.72

361

362 4.2 Spatial distribution patterns

363 The spatial distribution patterns of the loess sinkholes ~~have been~~were analyzed considering
364 their relationships with other geomorphic features (Fig. 3) and using spatial analysis and
365 statistics tools (Fig. 8). The detailed geomorphological map of the Sunjiacha basin reveals that
366 sinkholes are preferentially distributed in the following zones (Fig. 3): (1) the margins of the
367 deeply entrenched lower-middle section of the Sunjiacha trunk stream; (2) tributary gully
368 systems in the lower-middle part of the Sunjiacha basin; (3) landslides (slid mass and crown),
369 mostly associated with the trunk channel; and (4) man-made terraces. The ~~Kernel~~kernel density
370 model in Figure 8a shows low densities mainly associated with upper part of the Sunjiacha
371 basin, where the drainage network shows a lower degree of incision, and rounded divides
372 characterized by low local gradients. Overall, there is a good spatial correlation between
373 sinkholes and areas with high local topographic gradients and loess deposits disturbed by
374 landslides. The hot spot model based on sinkhole area shown in Figure 8b illustrates a
375 pronounced cluster of small sinkholes (cold spots in blue) associated with recent landslides in
376 the lower sector of the basin. Clustering of large sinkholes (hot spots in red) mainly occur along
377 the main drainages of tributary catchments in the lower part of the Sunjiacha basin.

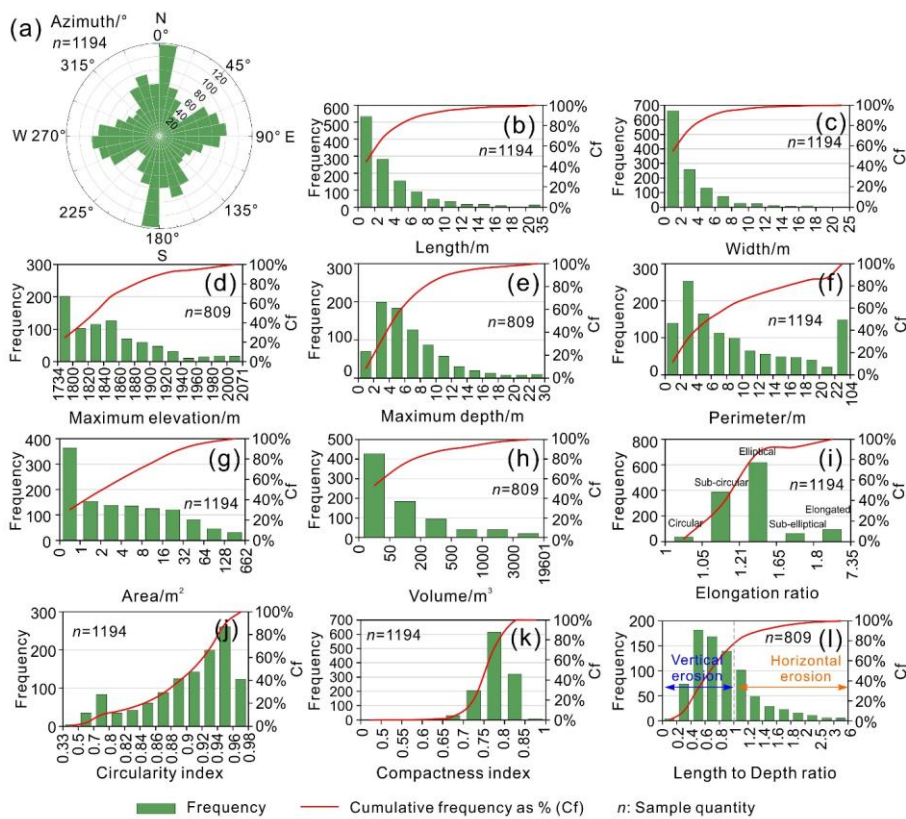


378
 379 **Figure 8.** Spatial distribution patterns of loess sinkholes: (a) Sinkhole type and kernel density
 380 map-Type and kernel density map (search radius: 100 m); (b) Hot spot map by sinkhole area
 381 (threshold distance: 100 m).

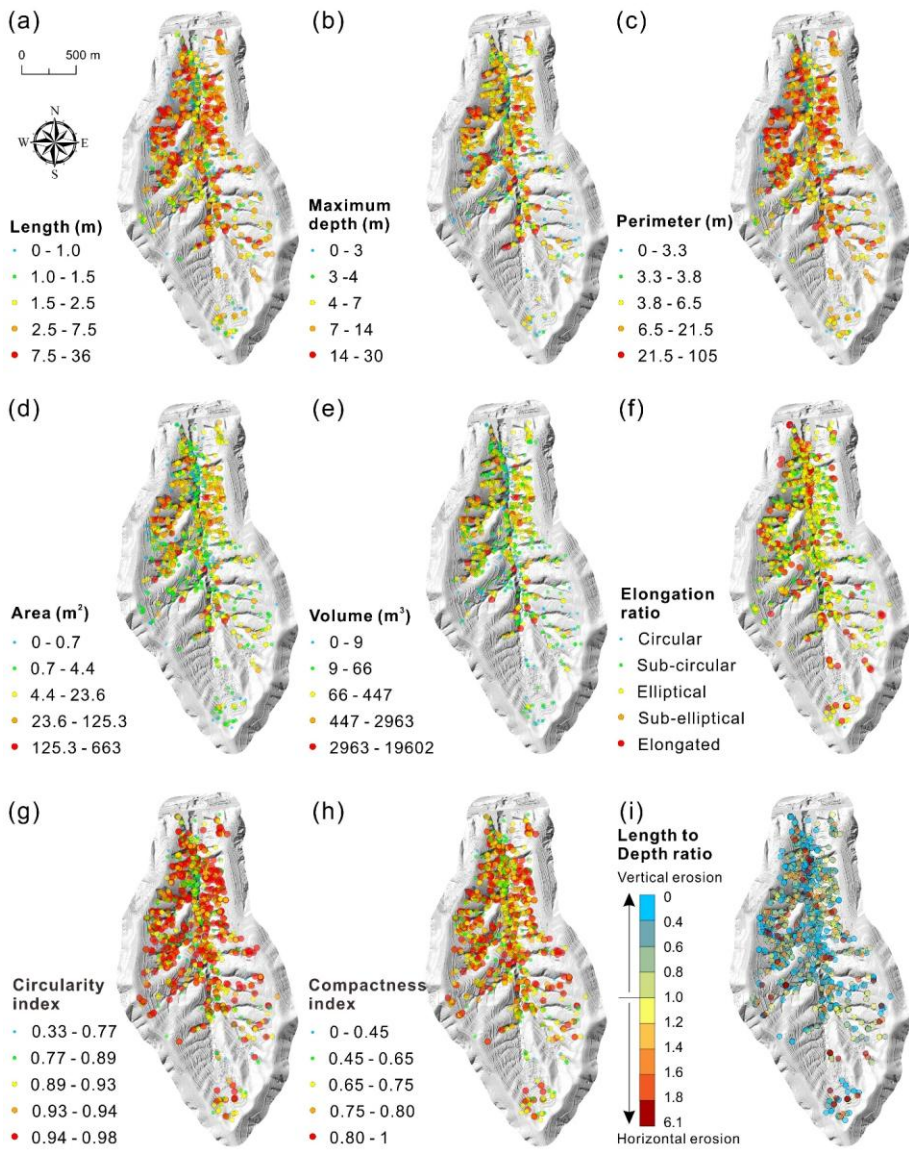
382 **4.3 Morphometric analysis**

383 In this section, Here below we analyze the spatial and morphometric parameters computed
 384 for the 1194 inventoried sinkholes (1162 single, 32 compound), their frequency-size
 385 distribution (Fig. 9), as well as some spatial patterns based on the distribution of different value
 386 ranges (Fig. 10). It should be noted that the airborne LiDAR returned sparse and limited point

387 clouds when detecting sinkholes with diameters less than 1 m. Consequently, for the calculation
 388 of parameters related to sinkhole depth and volume (e.g., Maximum Elevation, Maximum
 389 Depth, Volume, and Length-to-Depth Ratio), we retained only those 809 sinkholes with
 390 diameters ≥ 1 m.



391
 392 **Figure 9.** Frequency distribution, represented as number of sinkholes and cumulative
 393 frequency in percentage, of different spatial and morphometric parameters of the inventoried
 394 sinkholes: (a) Azimuth; (b) Length; (c) Width; (d) Maximum elevation; (e) Maximum depth;
 395 (f) Perimeter; (g) Area; (h) Volume; (i) Elongation ratio; (j) Circularity index; (k)
 396 Compactness index; (l) Length to Depth ratio.



397
 398 **Figure 10.** Spatial distribution of the sinkholes categorized into five different value ranges: (a)
 399 Length; (b) Maximum depth; (c) Perimeter; (d) Area; (e) Volume; (f) Elongation ratio; (g)
 400 Circularity index; (h) Compactness index; (i) Length to Depth ratio.

401 **4.3.1 Spatial parameters**

402 The ~~analyzed analyzed~~ spatial parameters include the orientation of the sinkholes (azimuth)
403 and the maximum elevation. The rose diagram in **Figure 9a** illustrates the frequency distribution
404 of the azimuth of the major axes of sinkholes, showing preferred N-S and W-E orientations.
405 The number of sinkholes in the Sunjiacha basin decreases as elevation increases (**Fig. 9d**). In
406 the relatively low elevation range of 1734~1860 m, there are 545 sinkholes (67.37%), whereas
407 while the number of sinkholes at mid-elevations (1860~1960 m) and high elevations
408 (1960~2071 m) are 216 (26.58%), and 48 (6.05%)~~in the relatively mid-elevation range of~~
409 ~~1860~1960 m, and in the high elevation range of 1960~2071 m are 216 (26.58%), and 48~~
410 ~~(6.05%)~~, respectively. Approximately 94% of the sinkholes are located in the more dissected
411 mid- and low- elevation areas, despite they represent 76% of the basin area.

412 **4.3.2 Planimetric morphometric parameters**

413 The analyzed planimetric morphometric parameters include length, width, perimeter, area,
414 elongation ratio, circularity index, and compactness index. The frequency distribution of the
415 length (**Fig. 9b**) and width (**Fig. 9c**) of sinkholes ~~follows~~exhibits a consistent pattern,
416 characterized by exponential decay as the values increase. The number of sinkholes with lengths
417 and widths ranging from 0 to 2 m is the highest, totaling 533 (44.64%) and 661 (55.36%),
418 respectively. Conversely, sinkholes exceeding 10 m in length and width account for only 7.45%
419 and 4.19% of the total sample, respectively. The map in **Figure 10a** reveals that sinkhole length
420 exhibits distinct~~shows some~~ spatial patterns, with smaller sinkholes preferentially occurring in
421 areas with lower degree of dissection (i.e., head of the basin and slopes close to the basin divides)

422 and in recent landslides associated with the trunk stream.

423 Regarding the ratio between length and width (elongation ratio, *ER*), [Basso et al. \(2013\)](#)
424 and [Zumpano et al. \(2019\)](#) classified the plan shape of sinkholes into five categories: circular
425 ($ER \leq 1.05$), sub-circular ($1.05 < ER \leq 1.21$), elliptical ($1.21 < ER \leq 1.65$), sub-elliptical
426 ($1.65 < ER \leq 1.8$), and elongated ($ER > 1.8$). [Figures 9i](#) and [10f](#) show that sinkholes tend to have
427 some degree of elongation, but without showing any clear spatial pattern in relation to this
428 parameter. Elliptical shapes dominate in the study area, with 618 sinkholes (51.76%), followed
429 by sub-circular morphologies with 384 depressions (32.16%). Elongated sinkholes also
430 represent a considerable number, totaling 93 (7.79%). Circular and sub-elliptical sinkholes are
431 relatively infrequent, with 35 (2.93%) and 64 (5.36%), respectively. ~~Similar to~~ Similarly to
432 length and width, the frequency of sinkhole perimeter and area shows a general decreasing trend
433 as the size increases ([Figs. 9f, g](#)). The maximum perimeter and area reach 104 m and 662 m²,
434 respectively. Sinkholes with a perimeter ≤ 4 m represent 21.9% (253) of the inventory, and 30.40%
435 are those with an area ≤ 1 m². In agreement with length and width, sinkholes with large perimeter
436 and area tend to occur ~~in~~ in sectors of the basin where the drainage net shows a greater degree
437 of entrenchment, with the exception of some recent landslides ([Figs. 8b, 10c, and 10d](#)).

438 The circularity index (*CLI*) quantitatively assesses how much the shape of a sinkhole
439 deviates from a perfect circle. CLI is equal to 1 in the case of a perfect circular shape and attains
440 progressively lower values as it becomes less circular (e.g., elongated, irregular edge). The
441 circularity index statistics indicate that 89.87% (1,073 sinkholes), 60.64% (724 sinkholes), and
442 10.30% (123 sinkholes) of the mapped sinkholes have a *CLI* greater than 0.8, 0.9, and 0.96,

443 respectively (Figs. 9j, 10g). The compactness index (*COI*) also quantifies how close is the shape
444 of the sinkhole perimeter to a circle. The elongation and/or complexity of the sinkhole perimeter
445 contributes to reduce the *COI* below 1. The loess sinkholes with a *COI* greater than 0.6, 0.7,
446 and 0.8 represent 99.58% (1189 sinkholes), 96.40% (1151 sinkholes), and 27.72% (331
447 sinkholes) of the sinkholes, respectively (Figs. 9k, 10h). The statistics of both the *CLI* and *COI*
448 reveal that the perimeter of a great proportion of the sinkholes significantly deviates ~~for~~ from a
449 circular shape, in agreement with the calculated elongation ratios. Moreover, these parameters
450 do not show any general ~~spatial cartographic~~ pattern, with the exception of a high proportion of
451 sinkholes with low *CLI* and *COI* values in some landslides associated with the trunk stream
452 (Figs. 10g, h).

453 4.3.3 3D morphometric parameters

454 The tThree-dimensional parameters are those that incorporate the vertical dimension,
455 including maximum depth, volume, and Length to Depth ratio. Note that large-area and large-
456 perimeter sinkholes may have reduced volume if their depth is low. The frequency distribution
457 of the maximum depth of the sinkholes in the study area shows a positively skewed distribution
458 (Fig. 9e). Sinkholes with depths ranging from 2 to 6 m represent 47.22% of the sample (382
459 sinkholes). Only 58 sinkholes exceed a maximum depth of 14 m, representing just 7.17% of the
460 total. The deepest sinkhole reaches a remarkable value of 29.6 m, and the average maximum
461 depth is 6.55 m~~The deepest sinkhole reaches and extraordinary value of 29.6 m and the average~~
462 ~~maximum depth is 6.55 m~~. The frequency of the sinkhole volume decreases exponentially as
463 the size increases, with maximum and average values of 19,601 m³ and 335 m³, respectively

464 (Fig. 9h). A total of 428 sinkholes (52.90%) have volumes of $\leq 50 \text{ m}^3$. The maps in Figures 10b
465 and 10e show that deeper sinkholes and large-volume sinkholes ($>500 \text{ m}^3$) preferentially occur
466 in association associated with deeply incised gullies.

467 To some extent, the length and depth of the sinkholes reflect the horizontal and vertical
468 development of the depressions, respectively. Thus, the Length to Depth ratio (LDr) indicates
469 whether sinkholes have greater horizontal ($LDr > 1$) or vertical ($LDr < 1$) dimension. The
470 relative value of these parameters can be influenced by multiple factors and processes, some
471 favoring greater lengths (e.g., sinkhole expansion, ~~sinkhole~~ coalescence) and others greater
472 depth (e.g., deep subsurface conduits, erosion at the floor of sinkhole with bottom outlet). The
473 frequency distribution of the LDr shows a positively skewed distribution, with 569 sinkholes
474 (70.33%) having a LDr lower than 1 (greater depth than length), while those with a LDr greater
475 than 1 represent 29.67% (240) of the sinkholes with depth data (Fig. 9I). These values indicate
476 that subsurface vertical erosion is the dominant process dominates in the formation of loess
477 sinkholes in the study area, largely due to the development of relatively deep pipes within the
478 thick loess cover (Fig. 10i).

479 4.4 Frequency-size relationships

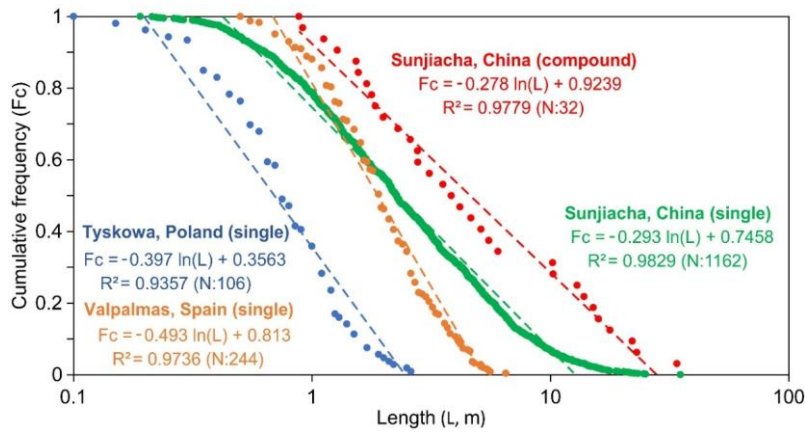
480 The semi-log plotgraph in Figure 11 represents separately the length of the 1162 single
481 sinkholes and the 32 compound sinkholes mapped in the Sunjiacha basin, versus relative
482 cumulative frequency. The latter indicates the frequency of sinkholes equal or larger than a
483 given length. The length distribution of the single sinkholes, ranging from 35.1 m to 0.2 m and
484 covering 2.3 orders of magnitude (i.e., $\log(\text{Max/Min})$), shows a wider range than the compound

设置了格式: 字体: 非倾斜

设置了格式: 字体: 非倾斜

485 sinkholes, spanning 1.6 orders of magnitude from 33.9 m to 0.9 m. As expected, compound
486 sinkholes tend to reach larger dimensions (i.e., plotted to the right), with a median length
487 (cumulative frequency = 0.5) that is 1.7 times larger than that of single sinkholes (3.8 m vs. 2.2
488 m), with a length value for the cumulative frequency of 0.5, 1.7 times larger than that of single
489 sinkholes (3.8 m vs. and 2.2 m).

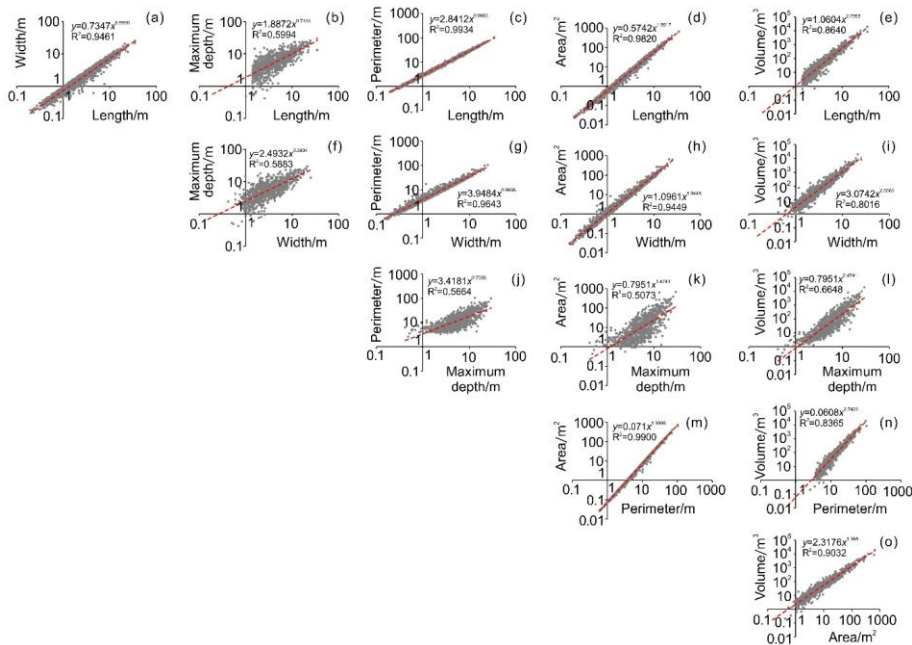
490 In both cases, the empirical cumulative frequency-size distribution can be modelled
491 satisfactorily by logarithmic functions (natural logarithm) with a high goodness of fit ($R^2 > 0.97$).
492 The regression of the compound sinkholes describes adequately the distribution for the whole
493 length range. In contrast, the empirical distribution of the single sinkholes deviates from the
494 fitted curve for both small (< 0.4 m) and large dimensions (> 12.7 m). These cut-off or rollover
495 points indicate lower empirical frequencies for the smaller sinkholes and higher frequencies for
496 the larger ones compared to the regression curve. ~~These cut-off or rollover points indicate lower~~
497 ~~empirical frequencies for the smaller sinkholes and higher empirical frequencies for the larger~~
498 ~~sinkholes than those shown by the regression.~~ Given the completeness of the sinkhole inventory,
499 the lower rollover can be attributed to physical constraints, such as the minimum span of a pipe-
500 roof required for a collapse to occur. The upper rollover could be related to factors such as the
501 expansion of single sinkholes and the depth distribution of sinkhole-forming underground pipes,
502 which in the study area can reach significant depths given the considerable~~high~~ thickness of the
503 loess cover. Note that sinkholes reach a maximum depth of 29.6 m.



504
 505 **Figure 11.** Graph showing the cumulative frequency-size distribution of single and compound
 506 sinkholes in the study area, as well as single piping sinkholes in other regions with different
 507 soils and environmental conditions (Tyskowa, Bieszczady Mountains, Poland; Valpalmas,
 508 Ebro Basin, NE Spain).

509 **4.5 Relationships between different parameters**

510 The planimetric (length, width, perimeter, area) and three-dimensional (maximum depth,
 511 volume) size parameters of the sinkholes were fitted pairwise in a matrix diagram showing
 512 graphically and with regressions (power functions) the relationships between each pair of
 513 morphometric parameters (Fig. 12). As expected, the regressions of pairs of planimetric
 514 parameters have always high goodness of fit $R^2 > 0.94$. In contrast, the relationship between
 515 planimetric and 3D parameters is poorer. R^2 is always below 0.6 for maximum depth, and less
 516 than 0.9 for volume, always <0.6 in the case of maximum depth, and lower than ≤ 0.9 in the case
 517 of volume.

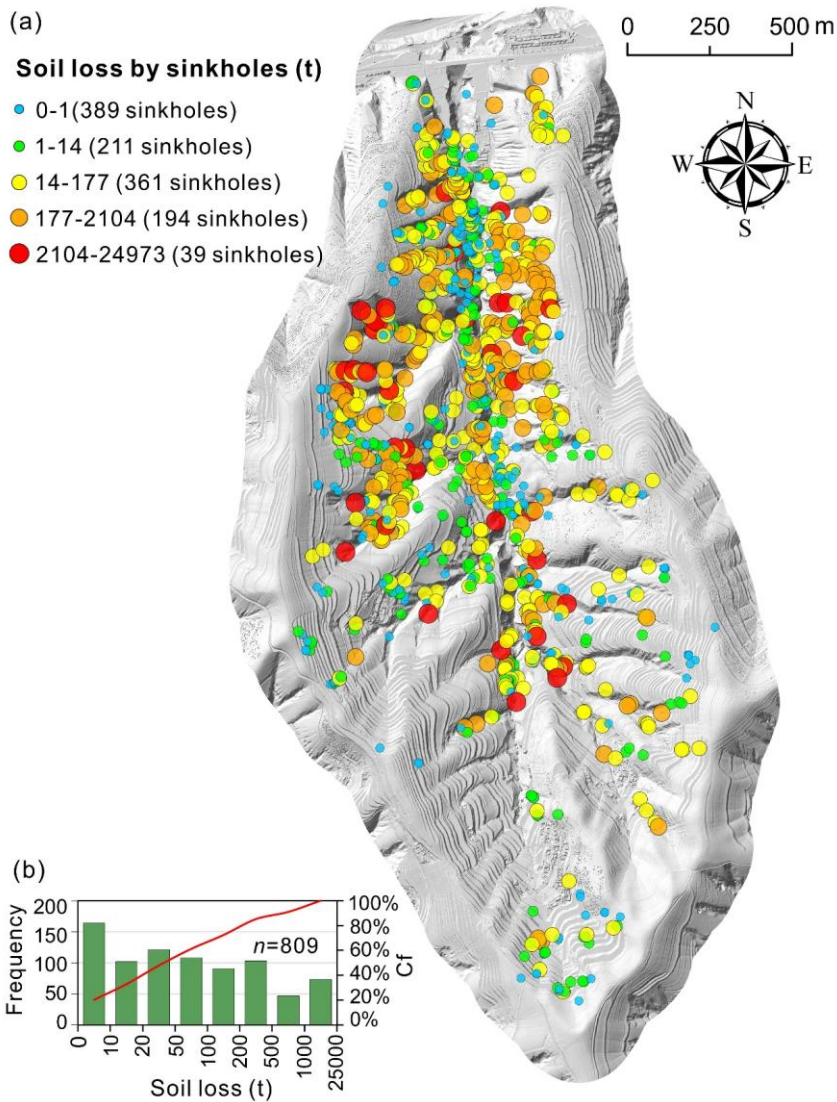


518
 519 **Figure 12.** Matrix diagram illustrating showing the pairwise fitting relationships of
 520 planimetric (length, width, perimeter, area) and 3D (maximum depth, volume) morphometric
 521 parameters.

522 4.6 Subsurface soil erosion

523 Sinkhole development, including cavity-roof collapse and the expansion of sinkhole
 524 margins by mass wasting processes, can contribute significantly to soil erosion, despite it is
 525 largely overlooked worldwide. The complete and accurate sinkhole inventory constructed in
 526 the Sunjiacha basin, including volumetric data, provides an excellent opportunity to assess the
 527 impact of sinkhole-related soil erosion within the context of the Loess Plateau. We calculated
 528 the soil loss associated with each sinkhole by multiplying the volume of each depression by the
 529 soil's dry bulk density, as shown in Figure 13a. Figure 13b illustrates the frequency distribution

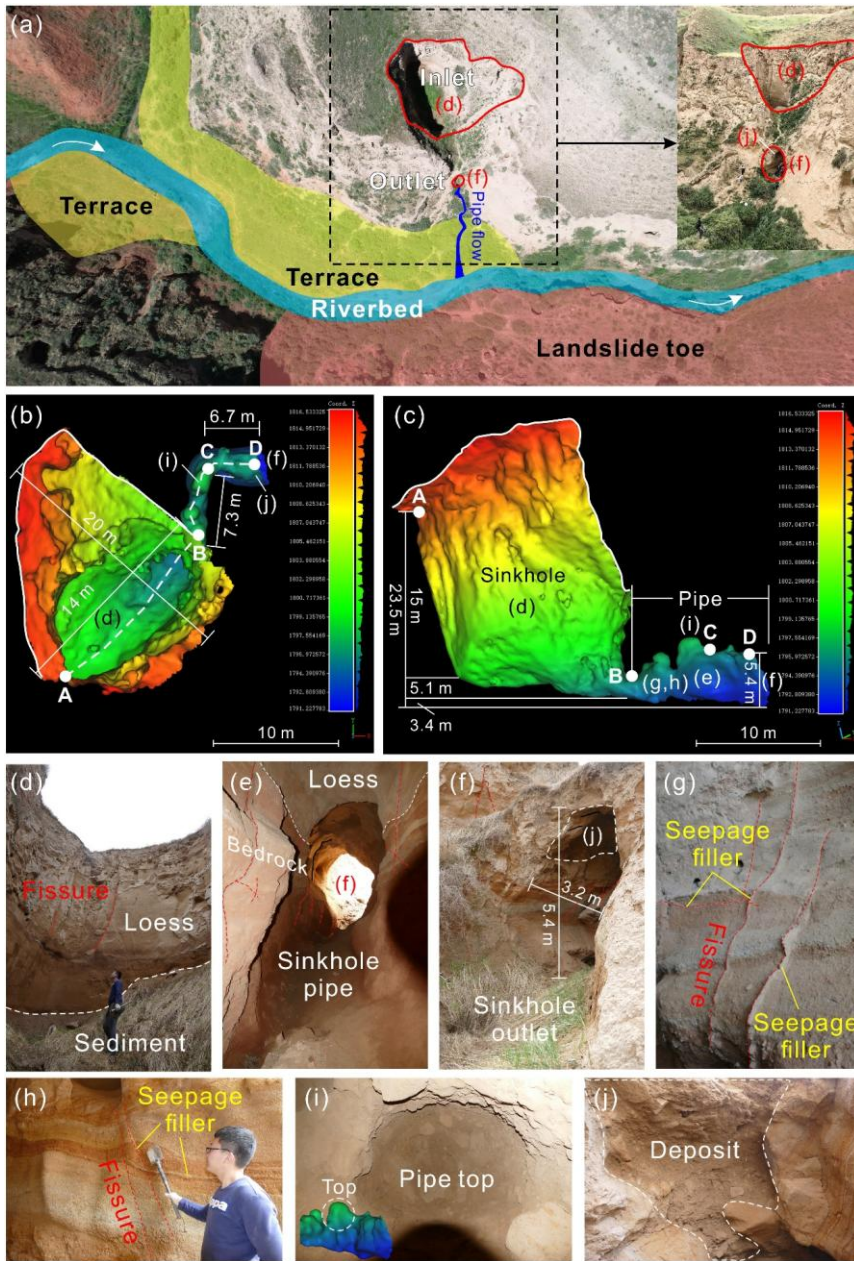
530 of soil loss related to individual sinkholes: 0~1 t (389 sinkholes, 32.58%); 1~14 t (211 sinkholes,
531 17.67%); 14~177 t (361 sinkholes, 30.23%); 177~2014 t (194 sinkholes, 16.25%); 2014~24973
532 t (39 sinkholes, 3.27%). The aggregate volume of sinkholes ($27.08 \times 10^4 \text{ m}^3$) multiplied by the
533 soil's dry bulk density (1.27 t/m^3) yields a total soil loss for the basin of $34.50 \times 10^4 \text{ t}$. Considering
534 the area of the basin (2400 ha), the specific soil erosion related to sinkholes can be estimated at
535 143.75 t/ha. Note that these values do not include hidden non-collapsed pipes. **Figure 13a** shows
536 that the impact of the process is quite uneven, with a much greater contribution in the lower
537 half of the basin and in the areas associated with deeply incised gullies.



538
 539 **Figure 13.** Soil loss by sinkholes—: (a) Spatial distribution map indicating soil erosion related
 540 to individual sinkholes; (b) Histogram and cumulative frequency (Cf) curve of soil loss for
 541 individual sinkholes. Frequency distribution histogram and cumulative frequency (Cf) curve of
 542 soil loss by individual sinkholes.

543 **4.7 In-depth investigation of a complex sinkhole**

544 Point clouds captured by airborne LiDAR surveys cover most of the sinkhole topography,
545 thanks to the vertical orientation of the sensors. However, obtaining comprehensive point
546 clouds of the interior of sinkholes ~~remains~~proves challenging due to line-of-sight obstructions
547 and the complex morphology~~obstructions and complex morphology~~. To address the limitations
548 of airborne LiDAR scanning, we employed a handheld laser scanner to conduct a detailed an
549 ~~in-depth~~ investigation in the interior of thirteen representative sinkholes. **Figures 14a-j** shows
550 the field photographs and 3D models of a loess sinkhole (HLS01). Morphometric measurements
551 indicate that the perimeter of the sinkhole at the land surface is 49.7 m, with an area of 179.6
552 m² and a maximum vertical depth of 20.1 m. We adopted both the traditional method and the
553 point cloud slicing algorithm to estimate the volume of this sinkhole. The results show a volume
554 and soil loss of 3610 m³ and 4585 t calculated by the former method, while the latter yielded
555 values of 1750 m³ and 2223 t, respectively (**Table 3**). ~~Because~~Due to the fact that the sinkhole
556 has an inclined top opening and a sloping bottom underlain by deposits (**Figs. 14a, d**), the
557 volume calculated by the traditional method was twice higher than the actual volume. This
558 finding also demonstrates~~proves~~ that handheld laser scanning can capture the complete
559 geometry of the sinkhole more accurately, overcoming the technical limitations of airborne
560 LiDAR~~capture more accurately the whole geometry of the sinkhole, overcoming the technical~~
561 ~~shortcomings of airborne LiDAR.~~

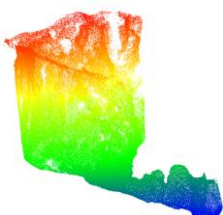
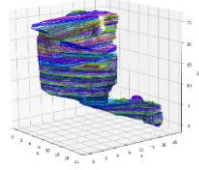


562
563

Figure 14. Detailed Investigation of the interior of a representative sinkhole

564 with an opening at the bottom (see [location in Figs. 5a and f](#)): (a) [Location, overview field](#)
 565 [photograph, and associated landforms](#)—[Location, general field view, and landforms](#); (b) 3D
 566 model generated from GeoSLAM point clouds, [annotated](#)~~labelled~~ with morphometric
 567 measurements; (c) Model slice along the AD profile line, [also showing](#)~~labelled with~~—
 568 morphometric measurements; (d) Photograph of the sinkhole bottom; (e) Photograph of the
 569 pipe; (f) Sinkhole outlet; (g-h) Bedrock exposed in the sinkhole wall; (i) Photograph of the
 570 pipe top; (j) Poorly-sorted deposits including angular loess clasts accumulated in the sinkhole
 571 floor by collapse and mass wasting processes.

572 **Table 3** Comparison of [sinkhole](#) volume and [corresponding](#) soil loss [estimated](#)
 573 [using](#)~~calculated by~~ traditional method [versus](#)~~and~~ point cloud slicing algorithm.

	Traditional method	Point cloud slicing algorithm
Data source	Airborne LiDAR	GeoSLAM LiDAR
Visualization		
	Vertical scanning by the UAS LiDAR	Multidirectional scanning by the handheld laser scanner.
Volume calculation principle	Volume= Area×Maximum depth (Gökkaya et al., 2021 ; De Waele and Gutiérrez, 2022)	 The convex hull algorithm is used to slice the point clouds at a thickness of 0.2 m. The volume of each slice is calculated and then summed up to obtain the total volume.
Soil loss (SL)	SL=ρ×V, where ρ is the dry density of soil, V is the volume of the sinkhole.	
Results	V: 3610 m ³ SL: 4585 t	V: 1750 m ³ (shaft 1606 m ³ , pipe 144 m ³)

574 Interestingly, most sinkholes examined in the field display dominant vertical development,
575 while this particular sinkhole exhibits a complex three-dimensional morphology comprising a
576 vertical shaft connected to a subhorizontal pipe. The upper shaft-like portion of the sinkhole
577 (20 m length \times 14 m width \times 20.1 m depth) is situated in loess deposits, while the lower portion
578 (14 m length \times 3.2 m width \times 5.4 m height) is a gently inclined ellipsoidal conduit carved into
579 horizontally bedded and jointed reddish sandstone. This lower conduit ends at the sinkhole
580 outlet perched 8 m above the valley floor (Fig. 14a). Unfortunately, due to the lack of precise
581 chronological evidence, we are unable to determine whether the initial development of this
582 sinkhole predates or postdates the valley incision. We interpret that the development of this
583 complex sinkhole started as a backward propagating conduit at the foot of the slope, associated
584 with a seepage outlet point controlled by joints in the loess cover and the bedrock (Figs. 14d-
585 h). Eventually, the enlarging conduit reached a sufficiently large span to initiate upward roof
586 collapse, ultimately originating the sinkhole. At present, five distinct ceiling cupolas can be
587 clearly observed at the top of this pipe (Figs. 14b, c and i), indicating sites of upward roof
588 propagation (stopping). ~~The incision of the drainage network within a context of rapid crustal~~
589 ~~uplift resulted in the sinkhole outlet being hanged 8 m above the current thalweg.~~

590 Additionally, we observed a significant accumulation of horizontally stratified flood
591 deposits resting atop the aeolian loess on the fluvial strath terrace (Fig. 14a). The interior of the
592 sinkhole is relatively cool and damp, with the bottom underlain by collapsed soil. We found
593 remnants of past flash-flood or debris-flow deposits on the sinkhole floor, as well as on the
594 walls and outlet ceiling of the connected lateral pipe (Figs. 14d, f, j). These sediments may

595 include: (1) Horizontally bedded deposits accumulated during floods in the drainage, with a
596 stage high enough to cause the penetration of flood waters into the sinkhole outlet
597 (backflooding); (2) Massive to poorly stratified deposits derived from collapse and mass
598 wasting processes acting primarily in the pipe roof and sinkholes margins, respectively. It
599 should be particularly noted that the largest loess landslide in this basin occurred on the opposite
600 bank of this sinkhole. Based on field investigations, we believe that this landslide completely
601 blocked the paleo-channel at that time, forming a small-scale dammed lake, and the landslide
602 deposits and lacustrine sediments could easily have entered the interior of the sinkhole through
603 lateral pipe.

604 **5 Discussion**

605 **5.1 Contributions of different factors to the sinkhole development–**

606 The development of loess sinkholes is influenced by multiple factors of different nature,
607 such as topography, climate, hydrology, soil texture, joints and fissures, animal activity, plant
608 root systems, and human activity (Bernatek-Jakiel and Poesen, 2018; Peng et al., 2018; Geng
609 et al., 2021; Hu et al., 2022; Kariminejad et al., 2023; Li et al., 2024). At the scale of a small
610 basin, climate exhibits minimal variation. Therefore, ~~We~~ focus our analysis on the
611 relationships between loess sinkholes and variables related to catchment topography,
612 geomorphology, hydrology, and land use. In order to better understand the controlling factors,
613 a number of topographic and geomorphic indices and variables, such as Slope, Total Catchment
614 Area (TCA), Topographic Wetness Index (TWI), Valley Depth (VD), Channel Network
615 Distance (CND), Landslides, and Landuse, were computed with the open-source SAGA GIS

616 platform and subsequently mapped in ArcMap 10.5 (Figs. 15a-g). The selection of these indices
617 and variables is primarily based on the following considerations: (1) Slope ~~governs~~~~provides~~ the
618 inherent hydraulic gradient conditions for rainfall infiltration and surface runoff concentration,
619 controlling the piping process leading to sinkhole development; (2) Total Catchment Area
620 ~~represents~~~~is~~ the upslope land surface that contributes surface and near-surface flow to a given
621 outlet, pixel, or stream segment (Gallant and Hutchinson, 2011). It is a proxy for the potential
622 volume of water that can reach a pipe or a sinkhole site, ~~influencing~~~~having influence~~ on their
623 initial formation and subsequent morphological evolution; (3) Topographic Wetness Index is a
624 steady-state, terrain-based proxy for soil moisture and surface saturation potential. It quantifies
625 the tendency of water to accumulate at any location by integrating local slope with the upslope
626 contributing area (Moore et al., 1991); (4) Valley Depth is a measure of the vertical distance
627 from a valley's highest ridges down to its lowest points. It is a proxy ~~of~~~~for~~ the degree of
628 dissection; (5) Channel Network Distance ~~represents~~~~is~~ the vertical height from a location to
629 the nearest stream. Its value on valley margins depends on both gradient and planimetric
630 distance to the nearest drainage; (6) Landslides can remodel the local topography and
631 significantly disturb loess deposits, reducing their mechanical strength and increasing their
632 permeability, which in turn ~~promotes~~~~favor~~ piping and sinkhole development; (7) Landuse
633 mainly reflects the impact of human activity, notably terracing, on piping and sinkhole
634 development.

635 In order to assess the spatial relationships between sinkholes and the different indices and
636 variables, we calculated normalized frequencies for different intervals. This normalized

637 frequency (F_n) is given by the ratio between the proportion of sinkholes in the interval and the
638 proportion of the area of that interval. The higher the value of this ‘likelihood ratio’, the higher
639 the spatial concurrence between sinkholes and the areas with values within the interval (Figs.
640 [15a1-g1](#)). These data, together with the findings presented in the results, [help to shed light on](#)
641 ~~contribute to shed light into~~ the formation and spatial distribution of the loess sinkholes.

642 Overall, the normalized frequency graphs show that the distribution of sinkholes is
643 primarily controlled by hydrological, topographic and geomorphic factors. Water availability is
644 an essential factor, in as much as subsurface flow is the geomorphic agent responsible for piping
645 development. This is illustrated by the higher normalized frequencies of sinkholes in areas with
646 high Total Catchment Area ($>100 \text{ m}^2$; $F_n=2.97$) and high Topographic Wetness Index (>9 ;
647 $F_n=4.92$). Slope is the main governing topographic factor, which largely determines hydraulic
648 gradient and the erosional capability of subsurface flow. Sinkholes preferentially occur in high
649 gradient areas and close to incised gullies, with high Slope ($>40^\circ$; $F_n=1.82$), high Valley Depth
650 ($>10 \text{ m}$; $F_n=1.98$), low Channel Network Distance ($<1 \text{ m}$; $F_n=1.98$), and areas primarily
651 classified as erosional gullies ($F_n=2.53$). A good spatial correlation is also observed between
652 sinkholes and landslides, with a normalized frequency of sinkholes within landslides ($F_n=3.42$).
653 These spatial patterns are clearly recognizable in the detailed geomorphological map (Fig. 3)
654 and the Kernel density (Fig. 8a) and hot spot maps (Fig. 8b). The latter shows that sinkholes
655 developed on landslides tend to be smaller. This could be attributed to a younger age of those
656 sinkholes, developed on a more recent geomorphic surface.

657 The vast majority of the sinkholes occur in erosional gullies (71.44%, 853 sinkholes). This

658 pattern is consistent with findings reported for soil pipes in other regions worldwide (Verachtert
659 et al., 2010; Kariminejad et al., 2023). Incised gullies may foster the development of pipes and
660 sinkholes through various mechanisms (Bernatek-Jakiel and Poesen, 2018; Peng et al., 2018):
661 (1) they create steep hydraulic gradients; (2) they guide converging surface and subsurface
662 drainage; (3) they favor the development of inlet points (e.g., unloading cracks) and outlet
663 points for seepage flow. As shown in Figures 6c-f, rows of sinkholes occur along the bottom of
664 erosional gullies. These sinkholes can be connected through groundwater seepage channels, as
665 confirmed by electrical resistivity tomography surveys in previous studies (Hu et al., 2022). It
666 can be anticipated that, with the expansion and coalescence of the sinkholes, the gully will
667 experience significant entrenchment and will turn into a drainage dominated by surface flow.

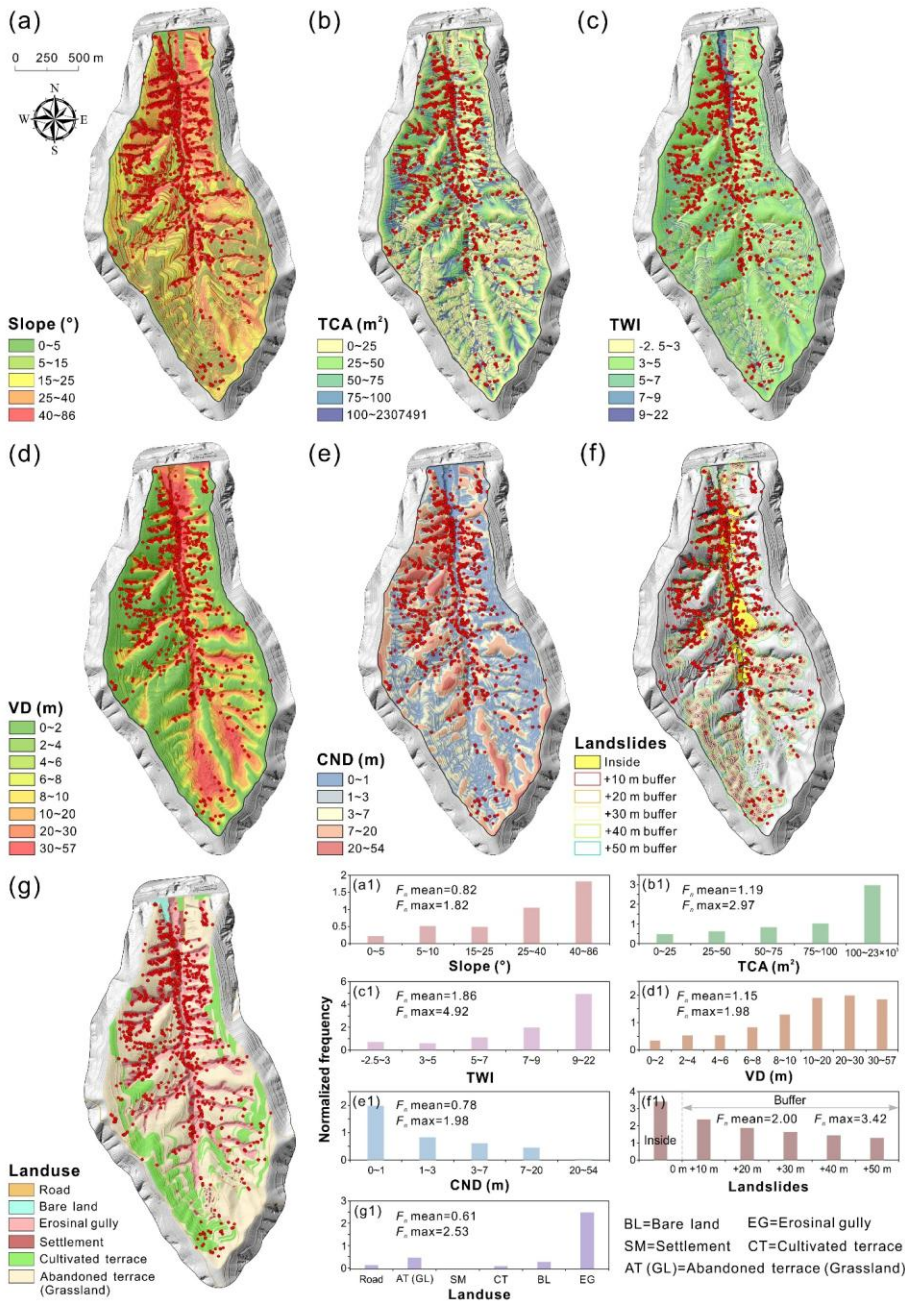
668 Another interesting feature is the close association between landslides and sinkholes in the
669 Sunjiacha basin. Previous studies have shown that soil pipes in slopes can favor efficient
670 drainage and, to some extent, help maintain slope stability (Pierson, 1983; Uchida et al., 2001;
671 Sidle and Bogaard, 2016). However, the sinkholes mapped on the landslides have mostly
672 formed after the development of the slope movements. The greater susceptibility of landslide
673 ground to piping and sinkhole development can be attributed to several factors: (1) landsliding
674 contributes to weaken the loess deposits; (2) the internal deformation of the landslide mass
675 typically involves a bulking effect (dilation and volume expansion) accompanied by an increase
676 in permeability~~permeability increase~~; and (3) fissures and other pathways for focused water
677 infiltration are common on landslides (Hu et al., 2020, 2022). At some sites, a causal
678 relationship between landslides and sinkholes can be inferred, showing a cascading geomorphic

679 effect. **Figures 15f and f1** illustrate that landslides play an important role in the development of
680 sinkholes. The distance to landslides seems to control the development of sinkholes, but this
681 control effect gradually decays with increasing distance from the landslide boundary. Statistics
682 show that as many as 251 sinkholes (accounting for 21%) have developed within the landslides,
683 making the landslide interior the second largest contributor to sinkhole formation ($F_n=3.42$).
684 Approximately 43% of sinkholes are distributed within the landslide and its outward 20m buffer
685 zone ($F_n=1.87$). The size of the sinkholes (e.g., length, area and volume), which can be
686 considered as a proxy for their age, seems to be influenced by the age of the geomorphic surface.
687 Mature sinkholes tend to be larger due to expansion and coalescence, and they usually occur on
688 old geomorphic surfaces (such as old gullies, river terraces and ancient landslides). Conversely,
689 sinkholes developed on landslides that have occurred in the past few years or decades tend to
690 be smaller. This pattern is clearly depicted in the hot spot map shown in **Figure 8b**.

691 We should be aware that the formation of soil pipes and sinkholes is not determined by a
692 single factor, but rather results from the interplay of interconnected geomorphic processes and
693 overlapping external influence factors (e.g., loess thickness, landscape position, surface and
694 subsurface flow, impermeable base layers, etc.). Conversely, the development of soil pipes and
695 sinkholes can further undermine slope stability, intensify gully erosion, and induce geological
696 hazards such as collapses, landslides, and debris flows.

697 In recent decades, due to a significant decrease in the local agricultural population and the
698 implementation of policies that promote the conversion of farmland back to forests and
699 grasslands, approximately 74% of the terraced fields have been taken out of

700 ~~cultivation~~~~abandoned for cultivation~~. The landuse map (Figs. 15g, g1) shows that abandoned
701 terraces have ~~reverted to~~~~evolved into~~ grasslands in the Sunjiacha basin. Abandoned terraces
702 (25.63%, 306 sinkholes) appear to be more prone to sinkhole formation than cultivated terraces
703 (2.51%, 30 sinkholes). This can be related to more favorable conditions for pipe development
704 in the abandoned terraces and the lower preservation potential of the sinkholes in the cultivated
705 terraces, where sinkholes tend to be filled soon after their formation. Without a doubt, pipe
706 collapses and gully development pose threats to land productivity, agricultural sustainability,
707 soil nutrient levels, and the carbon cycle, while also potentially destabilizing socio-economic
708 conditions (Llena et al., 2024). By contrast, roads, bare land, and settlement sites seem to exert
709 almost no influence on sinkhole occurrence.



711 **Figure 15.** Spatial relationships between sinkholes and different indices and variables
712 expressed as maps (a-g) and normalized frequency graphs—(a1-g1).

713 **5.2 Spatial and morphological features**

714 Sinkholes tend to be elongated and preferentially oriented in the Sunjiacha basin (Figs. 9a,
715 i). The majority of the major axes of the sinkholes align closely with the directions of the trunk
716 (N-S) and secondary (E-W) channels in the watershed (Fig. 3). These directions tend to guide:
717 (1) subsurface water flow and the trend of pipes generated by internal erosion, and (2) the
718 orientation of unloading cracks (e.g., scarped channel margins) through which water can
719 infiltrate. Both the pipes and the cracks influence the horizontal development of the sinkholes
720 by mass wasting processes acting ~~in~~on the margins and through coalescence (e.g., the merging
721 of aligned sinkholes connected to a common pipe).

722 The altitudinal distribution of sinkholes (Fig. 9d) may be governed by several factors: (1)
723 the density and entrenchment degree of the drainage network ~~is~~are higher at lower elevations;
724 (2) ground disturbed by landslides chiefly occurs ~~at~~in low elevation areas associated with the
725 trunk Sunjiacha stream; (3) high-elevation zones (e.g., rounded drainage divides) generally
726 have lower topographic gradient, lower degree of dissection, thinner loess cover, and more
727 restricted runoff contributing areas.

728 The deeper and larger sinkholes tend to be distributed in the more deeply incised ~~deeper~~
729 valleys (Figs. 10b, e). This pattern can be attributed to the development of deeper subsurface
730 pipes in areas with thicker loess, greater topographic gradient and lower local base level.
731 Thicker loess tends to accumulate in paleotopographic lows, which subsequently guide gully
732 networks.

733 The goodness of fit between the planimetric and 3D parameters of the sinkholes is
734 relatively poor (Fig. 12). This indicates a limited dependence between the horizontal and
735 vertical dimensions of sinkholes, in agreement with the wide range shown by the Length to
736 Depth ratio (0~6). That is, sinkholes with small area can have significant depth and volume,
737 and sinkholes with limited volume can reach relatively large areas. This is also reflected by the
738 relatively poor fit shown between the two 3D parameters (volume and maximum depth;
739 $R^2=0.66$). Even so, the fitting equations presented in Figure 12 provide preliminary empirical
740 support for characterizing and predicting scaling relationships for sinkholes in the Loess Plateau.

741 5.3 Frequency-size relationships of sinkholes in different soils and environments

742 The cumulative frequency-size graph in Figure 11 shows that the length distribution of the
743 compound sinkholes (red) is clearly ~~shifted~~~~displaced~~ towards larger dimensions with respect to
744 the single sinkholes (green). The average length of the compound and single sinkholes ~~are~~~~is~~
745 7.37 m and 3.65 m, respectively. This expected deviation in the size distribution can be
746 explained by the different sets of processes that operate in the development of the two sinkhole
747 populations. The size of the single sinkholes is related to pipe-roof collapse and the subsequent
748 expansion of the scarped edge of the depressions by erosional processes, mainly mass wasting
749 and gullyng. The size tends to increase with the time elapsed since the initial collapse, as the
750 sinkhole edge recedes. Compound sinkholes result from the coalescence of adjoining and
751 expanding sinkholes and/or the occurrence of a new sinkhole intersecting a pre-existing one,
752 leading to the sudden enlargement of the depressions. The contribution of these processes
753 (coalescence, intersection) is influenced by the density and clustering degree of the sinkholes,

754 in as much as the likelihood of sinkhole aggregation is greater in tightly clustered sinkhole
755 populations (Bernatek-Jakiel et al., 2019; De Waele and Gutiérrez, 2022; Sevil and Gutiérrez,
756 2023). Moreover, sinkhole merging entails a decrease in sinkhole density by number and a
757 substantial increase in sinkhole size.

758 **Figure 11** shows the cumulative frequency-length distribution of the single and compound
759 sinkholes mapped in the Sunjiacha basin, together with the single sinkholes inventoried in two
760 catchments with contrasting geological and climatic conditions (Bernatek-Jakiel et al., 2019):
761 Valpalmas in the Ebro Cenozoic Basin (NE Spain), and Tyskowa in the Bieszczady Mountains
762 of the Outer Eastern Carpathians (Poland). The pipe collapses in Valpalmas occur in Holocene
763 valley-fill alluvium consisting of indurated ~~and~~ Na-rich cohesive clayey silt that reaches
764 around 8 m in thickness. Here, the climate is semiarid (mean precipitation 500 mm) and
765 sinkholes tend to occur associated with the edge of erosional scarps, showing a tightly clustered
766 distribution. The pipe collapses in the Tyskowa catchment can be considered as a representative
767 sample of those inventoried in several catchments of the ~~Bieszczady~~ Bieszczady Mts.,
768 characterized by a humid climate (mean precipitation 900 m; Bernatek-Jakiel et al., 2019). Here,
769 sinkholes occur on relatively thin slope deposits with some eolian component consisting of
770 poorly indurated clayey silt. The single sinkholes in Valpalmas (orange) show a similar size to
771 the single sinkholes in Sunjiacha for the central cumulative frequencies (i.e., F_c 0.5~0.6).
772 Nonetheless, single sinkholes in Valpalmas display a much narrower length range (1.1 ~~vs.~~
773 2.3 orders of magnitude, resulting in steeper curve) and significantly smaller maximum
774 dimensions (6.5 m vs. 35.1 m). The more restricted size range ~~of~~ for the smaller sinkholes can

775 be attributed to the fact that the inventory in Valpalmas was ~~restricted~~restricted to sinkholes
776 with lengths ≥ 0.5 m. The differences between Sunjiacha and Valpalmas can be ascribed to
777 factors such as the greater morpho-sedimentary diversity of Sunjiacha, where sinkholes occur
778 in a broad range of deposits and geomorphic settings (e.g., loess, colluvium, alluvium), and the
779 wide depth range of sinkhole-forming pipes, substantiated by the measured maximum depth of
780 the sinkholes, ranging from 29.6 to 0.42 m (Figs. 9e, 10b and 14c). Single sinkholes in the
781 humid ~~Bieszczady~~Bieszczady Mts. of Poland are much smaller, mainly because they occur
782 on thinner and mechanically weaker deposits. The weaker the soils, the smaller the largest span
783 that can reach cavities before collapse. Induration of the deposits by secondary carbonate (i.e.,
784 cementation) in this humid environment is less significant ~~that~~than in the semiarid
785 environments of ~~Valpalmas~~Valpamas and the Loess Plateau.

786 5.4 Limitations and prospects

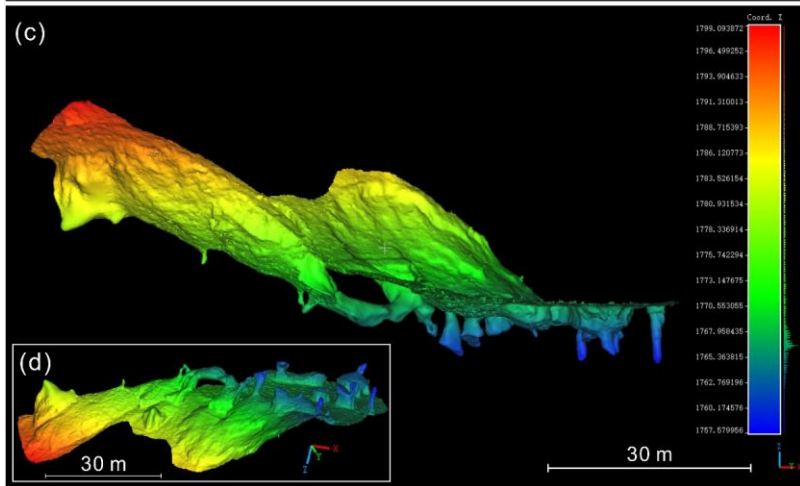
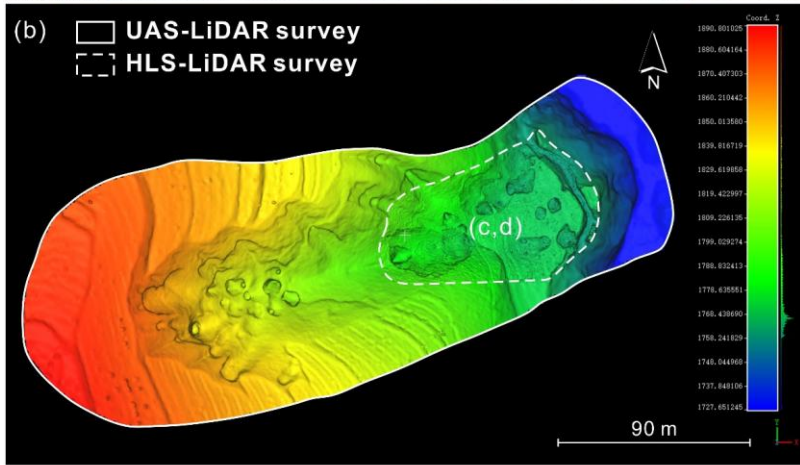
787 Extensive field surveys reveal that loess sinkholes possess highly complex three-
788 dimensional morphologies, rather than ~~being a~~simple cylindrical or conical ~~features~~shape (Figs.
789 6i, 7c, 14b and 16; Hu et al., 2024). This is illustrated by the high-resolution scanning of 142
790 sinkholes with a handheld laser device carried out in 2021 in a small basin, named Laozigou,
791 east of our study area (Hu et al., 2024; Jiang et al., 2024). The data can be accessed at
792 <https://doi.org/10.1016/j.geomorph.2024.109404>. As shown in Table 3, volume estimates based
793 on airborne LiDAR point clouds and simplified volume estimation methods can lead to highly
794 inaccurate approximations. The aggregate volume, and hence the inferred soil loss reported in
795 our study area may therefore be overestimated. Several factors may contribute to the deviation

设置了格式: 非突出显示

796 between the actual volume and the volume calculated, leading to over- or under-estimations: (1)
797 volumes are calculated using maximum depth and assuming a cylindrical geometry, but
798 sinkholes may be conical (overestimation) or the actual depth may be deeper (underestimation);
799 (2) sinkholes may be connected to conduits that cannot be imaged in airborne surveys, resulting
800 in underestimations.

801 Encouragingly, the comprehensive point clouds acquired by the handheld scanner enable
802 us to develop far more precise cloud-slicing and volumetric-integration algorithms for exact
803 volume computation (Hu et al., 2024). This will enable us to develop a more reliable fitting
804 formula relating sinkhole area and volume, which could be used for refining the results obtained
805 from the UAS surveys. We conducted a survey of a gully by jointly employing UAS-LiDAR
806 and HLS--LiDAR technologies and found that the integrated point cloud data can effectively
807 delineate the internal structure and connectivity of sinkholes, as they overcome the limitations
808 of a single LiDAR technology. Meanwhile, machine-learning approaches for the automatic
809 detection and delineation of sinkholes are rapidly emerging and showing promising results (Zhu
810 et al., 2016, 2020; Jiang et al., 2024; Li et al., 2024; Coşkuner et al., 2025; Creati et al., 2025).
811 Indeed, we have already implemented an end-to-end workflow that couples airborne LiDAR
812 point clouds with deep-learning models to achieve automatic sinkhole identification, instance
813 segmentation, feature extraction, cataloguing, and mapping (Li et al., 2025) (Li et al., 2025, in
814 press).

设置了格式: 字体颜色: 红色



816 **Figure 16.** ~~Integrated sinkhole investigation combining UAS-LiDAR and HLS-~~
 817 ~~LiDAR~~ Sinkhole investigations by jointly using UAS LiDAR and HLS LiDAR: (a) ~~Coverage~~
 818 ~~areas of the two LiDAR surveys~~ The survey areas of the two LiDAR devices; (b) The mesh
 819 model generated from the ~~fused~~ merged point cloud data; (c) The side view of mesh model ~~of~~
 820 ~~from the~~ HLS-LiDAR survey area; (d) The bottom view of c.

821 6 Data availability

822 The dataset supporting this study is openly available on Zenodo at
 823 <https://doi.org/10.5281/zenodo.14000267> (Hu et al., 2025).

824 7 Conclusions

825 High-resolution models derived from photographs and LiDAR data captured with a UAS
 826 have allowed the production of a comprehensive cartographic inventory of loess sinkholes in a
 827 catchment (2.4 km²) of the Chinese Loess Plateau with a high density of sinkholes (ca. 500
 828 sinkholes/km²). The spatial data, including a bare-surface digital ~~elevation~~ surface model and a
 829 3D terrain point cloud, ~~proved suitable~~ was appropriate for for accurately mapping the sinkholes,
 830 differentiating between single (1194) and compound depressions (288), and extracting precise
 831 planimetric morphometric parameters. This is the first morphometric dataset available for the
 832 piping-related sinkholes of the ~~Chinese Loess Plateau~~ CLP. Three dimensional parameters such
 833 as depth and volume can be also extracted or estimated, although with much higher uncertainty.
 834 Rough cumulative volume estimates yield sinkhole-related soil erosion values of around 140
 835 t/ha. The work illustrates that the limitations of the airborne data for measuring 3D
 836 morphometric parameters can be overcome by using SLAM-based handheld scanners. The 3D
 837 point clouds obtained with these devices at specific sinkholes, although labor intensive, allow

838 ~~precise measurement of~~ ~~measuring precisely~~ the volume of the scanned voids. Nonetheless,
839 hidden pipes, which may account for a significant volume of subsurface erosion, remain elusive
840 for these direct surveying techniques.

841 The sinkholes in the analyzed catchment tend to be elongated (52% with elongation ratio
842 ~~between 1.21 and 1.65~~ ~~1.21-1.65~~) and preferentially oriented following the dominant trends of
843 the drainage network. They show a broad range of dimensions, ranging from 0.19 to 35.11 m
844 in length (2.3 orders of magnitude). As expected, compound sinkholes tend to be significantly
845 larger ~~that than~~ single sinkholes (7.37 m ~~versus~~ 3.65 m in average length, respectively),
846 although the degree of coalescence is rather moderate (single 97.3%; compound 2.7%). A
847 remarkable feature of the investigated sinkholes is their large vertical dimension. Around 70%
848 of the sinkholes ~~have a greater depth than length~~ ~~are deeper than longer~~. The average and
849 maximum depths are 6.5 m and 29.6 m, respectively, indicating the development of deep-seated
850 pipes in thick loess cover or even within the jointed and friable sandstone bedrock. Comparison
851 with other morphometric datasets from semiarid Spain (fine grained alluvium) and humid
852 Poland (thin loess-rich colluvium) reinforces the large size of the studied sinkholes in the
853 Chinese loess, developed on much thicker loess and generally rooted in deeper pipes. ~~The~~
854 ~~frequency size relationships produced could be transformed in sinkhole hazard curves~~
855 ~~incorporating the time dimension (i.e., timing of sinkhole occurrence).~~

856 The spatial relationships between the sinkholes and other geomorphic features and various
857 topographic and hydrologic indices reveal that their development is mainly controlled by the
858 amount of water available for subsurface flow (i.e., runoff contributing area) and topographic

859 gradient. Sinkholes occur preferentially along the steep margins of deeply incised streams and
860 gully networks. ~~Sinkhole preferentially occur associated with the steep margins of deeply~~
861 ~~incised streams and gully networks.~~ Recent landslides, underlain by weakened and more porous
862 disturbed loess deposits are also identified as areas especially prone to piping and sinkhole
863 occurrence.

864 **Author contributions.**

865 SH, FG, FZ, and SL designed the study and wrote the manuscript. SH, FG, and SL
866 compiled and analyzed the dataset. SH, XW, JS, and SW performed field investigation. NW,
867 XL, and FG supervised and reviewed the manuscript. All authors contributed to the writing and
868 editing of this paper.

869 **Competing interests.**

870 The contact author has declared that neither they nor their co-authors have any competing
871 interests.

872 **Disclaimer.**

873 Publisher's note: Copernicus Publications remains neutral with regard to jurisdictional
874 claims in published maps and institutional affiliations

875 **Acknowledgements.**

876 The authors are grateful to Dr. Anita Bernatek-Jakiel for providing published
877 morphometric data on piping sinkholes in the Valpalmas (Spain) and the Tyskowa (Poland)
878 catchments. The work by FG has been supported by the project DIAPERNO (PID2021-
879 123189NB-I00) of the Spanish Government (Ministerio de Ciencia e Innovación). FG belongs

880 to the IUCA and the Geoenvironmental Processes and Global Change (E02_23R) research
881 group financed by the Aragón Government and the European Social Fund (ESF-FSE). We
882 would also like to thank Dr. Yixian Chen for his participation in the fieldwork.

883 **Financial support.**

884 This research has been supported by the National Natural Science Foundation of China
885 (grant nos. 42371009, 42001006 and 42230712), the National Key Research and Development
886 Program of China (grant nos. 2022YFC3003401 and 2023YFC3008401).

887 **Review statement.**

888 This paper was edited by Giulio G.R. Iovine ~~XX~~ and reviewed by Christian Sommer ~~XX~~
889 and one anonymous referee.

890 **References**

- 891 Basso, A., Bruno, E., Parise, M., and Pepe, M.: Morphometric analysis of sinkholes in a karst
892 coastal area of southern Apulia (Italy), *Environ. Earth Sci*, 70, 2545–2559, 2013.
- 893 Bernatek, A.: The Influence of Piping on Mid-Mountain Relief: A Case Study from the Polish
894 Bieszczady Mts. (Eastern Carpathians), *Carpath J Earth Env*, 10, 107–120, 2015.
- 895 Bernatek-Jakiel, A., Jakiel, M., and Krzemiń, K.: Piping dynamics in mid-altitude mountains
896 under a temperate climate: Bieszczady Mountains, eastern Carpathians, *Earth Surf Proc*
897 *Land*, 42, 1419–1433, 10.1002/esp.4160, 2017.
- 898 Bernatek-Jakiel, A. and Kondracka, M.: Combining geomorphological mapping and near
899 surface geophysics (GPR and ERT) to study piping systems, *Geomorphology*, 274, 193–
900 209, 2016.
- 901 Bernatek-Jakiel, A. and Poesen, J.: Subsurface erosion by soil piping: significance and research
902 needs, *Earth-Sci Rev*, 185, 1107–1128, 10.1016/j.earscirev.2018.08.006, 2018.
- 903 Bernatek-Jakiel, A., Gutiérrez, F., Nadal-Romero, E., and Jakiel, M.: Exploring the frequency-

904 size relationships of pipe collapses in different morphoclimatic regions, *Geomorphology*,
905 345, 106845, 10.1016/j.geomorph.2019.106845, 2019.

906 Borah, U. K., Gond, A., Rajan, P. P., Sivan, R., and Vivekanandan, N.: Joint geomorphological
907 and geophysical (electrical resistivity) investigation for the configuration of soil pipe,
908 *Contrib Geophys Geod*, 52, 239–255, 10.31577/congeo.2022.52.2.4, 2022.

909 ~~Bruno Belme~~, E., Calcaterra, D., and Parise, M.: Development and morphometry of sinkholes
910 in coastal plains of Apulia, southern Italy. Preliminary sinkhole susceptibility assessment,
911 *Eng Geol*, 99, 198–209, 10.1016/j.enggeo.2007.11.017, 2008.

912 Cole, J. P.: Study of major and minor civil divisions in political geography, The 20th
913 international geographical congress, London, 1964.

914 Coskuner, B., İnce, İ., and Barstuğan, M.: Sinkhole detection via deep learning using DEM
915 images, *Nat Hazards*, 121, 8347–8366, 10.1007/s11069-025-07127-0, 2025.

916 Creati, N., Paganini, P., Sterzai, P., and Pavan, A.: Mapping of karst sinkholes from LIDAR
917 data using machine-learning methods in the Trieste area, *J Spat Sci*, 70, 365–380,
918 10.1080/14498596.2025.2469176, 2025.

919 Day, M.: Doline morphology and development in Barbados, *Annals of the Association of*
920 *American Geographers*, 73, 206–219, 1983.

921 De Carvalho Júnior, O. A., Guimarães, R. F., Montgomery, D. R., Gillespie, A. R., Gomes, R.
922 A. T., De Souza Martins, É. D., and Silva, N. C.: Karst Depression Detection Using
923 ASTER, ALOS/PRISM and SRTM-Derived Digital Elevation Models in the Bambu
924 Group, Brazil, *Remote Sens*, 6, 330–351, 10.3390/rs6010330, 2014.

925 De Waele, J. and Gutiérrez, F.: *Karst hydrogeology, geomorphology and caves*, John Wiley &
926 Sons, 888 p, 2022.

927 Donnelly, L. J.: Subsidence and associated ground movements on the Pennines, northern
928 England, *Q J Eng Geol Hydroge*, 41, 315–332, Doi 10.1144/1470-9236/07-216, 2008.

929 Farrant, A. R. and Cooper, A. H.: Karst geohazards in the UK: the use of digital data for hazard
930 management, *Q J Eng Geol Hydroge*, 41, 339–356, Doi 10.1144/1470-9236/07-201, 2008.

931 Gallant, J. C. and Hutchinson, M. F.: A differential equation for specific catchment area, *Water*

932 Resour Res, 47, W05535, 10.1029/2009wr008540, 2011.

933 Gao, Y., Alexander, E. J. R., and Barnes, R. J.: Karst database implementation in Minnesota:
934 analysis of sinkhole distribution, *Environ Geol*, 47, 1083–1098, 10.1007/s00254-005-
935 1241-2, 2005.

936 Gao, Y., Alexander, E.C., Tipping, R.: The development of a karst feature database for
937 southeastern Minnesota. *J. Cave Karst Stud.* 64, 51–57, 2002.

938 Geng, H. P., Liu, R., Zheng, W. S., Zhang, Y. B., Xie, R., Guo, Y., and Pan, B. T.: Interaction
939 Between Animal Burrowing and Loess Cave Formation in the Chinese Loess Plateau,
940 *Front Earth Sci*, 9, 806921, 10.3389/feart.2021.806921, 2021.

941 Geng, H. P., Xu, W. Y., Zheng, W. S., Gao, X. L., and Pan, B. T.: A hybrid mechanism for the
942 initiation and expansion of loess caves across the Chinese Loess Plateau, *Land Degrad*
943 *Dev*, 34, 3329–3339, 10.1002/ldr.4686, 2023.

944 Gibbs, H.S.: Tunnel-gully erosion on the Wither Hills, Marlborough. *New Zealand Journal of*
945 *Science and Technology* 27(A2), 135–146, 1945.

946 Gökkaya, E., Gutiérrez, F., Ferk, M., and Görüm, T.: Sinkhole development in the Sivas gypsum
947 karst, Turkey, *Geomorphology*, 386, 107746, 10.1016/j.geomorph.2021.107746, 2021.

948 Gutiérrez, F., Desir, G., and Gutiérrez, M.: Causes of the catastrophic failure of an earth dam
949 built on gypsiferous alluvium and dispersive clays (Altorricón, Huesca Province, NE
950 Spain), *Environ Geol*, 43, 842–851, 10.1007/s00254-002-0700-2, 2003.

951 Gutiérrez, F., Parise, M., De Waele, J., and Jourde, H.: A review on natural and human-induced
952 geohazards and impacts in karst, *Earth-Sci Rev*, 138, 61–88,
953 10.1016/j.earscirev.2014.08.002, 2014.

954 Hofierka, J., Gallay, M., Bandura, P., and Šašak, J.: Identification of karst sinkholes in a forested
955 karst landscape using airborne laser scanning data and water flow analysis,
956 *Geomorphology*, 308, 265–277, 10.1016/j.geomorph.2018.02.004, 2018.

957 Hu, S., Gutiérrez, F., Zhang, F., Li, S., Wang, N., Li, X., and Wang, X.: A morphological dataset
958 of loess sinkholes from a small basin in the Chinese Loess Plateau (1.0) [Data set]. Zenodo.
959 <https://doi.org/10.5281/zenodo.14000267>, 2025.

960 Hu, S., Jiang, Z.D., Wang, N.L., Zhang, F.Y., Chen, Y.X., Wu, S.B., Wang, L., Li, S.S.: In Situ
961 Dataset of Loess Sinkholes using UAS and LiDAR Technology in Huining County, China
962 (2024). Digital Journal of Global Change Data Repository,
963 <https://doi.org/10.3974/geodb.2024.05.05.V1>, 2024.

964 Hu, S., Qiu, H. J., Wang, N. L., Cui, Y. F., Wang, J. D., Wang, X. G., Ma, S. Y., Yang, D. D.,
965 and Cao, M. M.: The influence of loess cave development upon landslides and
966 geomorphologic evolution: A case study from the northwest Loess Plateau, China,
967 *Geomorphology*, 359, 107167, [10.1016/j.geomorph.2020.107167](https://doi.org/10.1016/j.geomorph.2020.107167), 2020.

968 Hu, S., Qiu, H. J., Wang, N. L., Wang, X. G., Ma, S. Y., Yang, D. D., Wei, N., Liu, Z. J., Shen,
969 Y. D., Cao, M. M., and Song, Z. P.: Movement process, geomorphological changes, and
970 influencing factors of a reactivated loess landslide on the right bank of the middle of the
971 Yellow River, China, *Landslides*, 19, 1265–1295, [10.1007/s10346-022-01856-0](https://doi.org/10.1007/s10346-022-01856-0), 2022.

972 Jiang, Z. D., Hu, S., Deng, H., Wang, N. L., Zhang, F. Y., Wang, L., Wu, S. B., Wang, X. A.,
973 Cao, Z. W., Chen, Y. X., and Li, S. S.: Detection and automatic identification of loess
974 sinkholes from the perspective of LiDAR point clouds and deep learning algorithm,
975 *Geomorphology*, 465, 109404, [10.1016/j.geomorph.2024.109404](https://doi.org/10.1016/j.geomorph.2024.109404), 2024.

976 Jones, E. and Beck, D.: The use of three-dimensional laser scanning for deformation monitoring
977 in underground mines, *Proceedings of the 13th AusIMM Underground Operators
978 Conference*: 66, 267–270, 2017.

979 Kariminejad, N., Sepehr, A., Poesen, J., and Hassanli, A.: Combining UAV remote sensing and
980 pedological analyses to better understand soil piping erosion, *Geoderma*, 429, 116267,
981 [10.1016/j.geoderma.2022.116267](https://doi.org/10.1016/j.geoderma.2022.116267), 2023.

982 Kim, C. E. and Anderson, T. A.: Digital disks and a digital compactness measure, *Proceedings
983 of the sixteenth annual ACM symposium on Theory of computing*, ACM Press, New York,
984 117–124, 1984.

985 Kobal, M., Bertoneclj, I., Pirotti, F., Dakskobler, I., and Kutnar, L.: Using Lidar Data to Analyse
986 Sinkhole Characteristics Relevant for Understory Vegetation under Forest Cover-Case
987 Study of a High Karst Area in the Dinaric Mountains, *Plos One*, 10, e0122070,

- 988 10.1371/journal.pone.0122070, 2015.
- 989 Konsolaki, A., Vassilakis, E., Gouliotis, L., Kontostavlos, G., and Giannopoulos, V.: High
990 Resolution Digital 3d Modelling of Subsurface Morphological Structures of Koutouki
991 Cave, Greece, *Acta Carsologica*, 49, 163–177, 10.3986/ac.v49i2-3.7708, 2020.
- 992 Lee, E. J., Shin, S. Y., Ko, B. C., and Chang, C.: Early sinkhole detection using a drone-based
993 thermal camera and image processing, *Infrared Phys Techn*, 78, 223–232,
994 10.1016/j.infrared.2016.08.009, 2016.
- 995 [Li, S., Sun, J., Hu, S., & Wang, L. \(2025\). LSPNet for Automatic Recognition and Cataloguing](#)
996 [of Loess Sinkholes from Point Clouds \(V1.0\). Zenodo.](#)
997 <https://doi.org/10.5281/zenodo.17667244>[Li, S., Hu, S., Wang, L., Sun, J., Zhang, F., Wang,](#)
998 [N., Wang, X., Wu, S., Xu, Z., and Pang, G.: LSPNet: Automatic Identification and](#)
999 [Segmentation of Loess Sinkholes in 3D Point Clouds Using an Enhanced PointNet++,](#)
1000 [Available at SSRN 5414065,](#)
1001 <https://papers.ssrn.com/sol3/Delivery.cfm?abstractid=5414065>, 2025
- 1002 Li, S. S., Hu, S., Wang, L., Zhang, F. Y., Wang, N. L., Wu, S. B., Wang, X. A., and Jiang, Z. D.:
1003 Quantifying the Geomorphological Susceptibility of the Piping Erosion in Loess Using
1004 LiDAR-Derived DEM and Machine Learning Methods, *Remote Sens*, 16, 4203,
1005 10.3390/rs16224203, 2024.
- 1006 Li, W. W., Goodchild, M. F., and Church, R.: An efficient measure of compactness for two-
1007 dimensional shapes and its application in regionalization problems, *Int J Geogr Inf Sci*, 27,
1008 1227–1250, 10.1080/13658816.2012.752093, 2013.
- 1009 Li, X., Song, Y., and Ye, W.: Engineering geological research on tunnel-erosion in loess, Tongji
1010 University Press, Shanghai, 2010. (in Chinese)
- 1011 Li, X. A., Wang, L., Hong, B., Li, L. C., Liu, J., and Lei, H. N.: Erosion characteristics of loess
1012 tunnels on the Loess Plateau: A field investigation and experimental study, *Earth Surf Proc*
1013 *Land*, 45, 1945–1958, 10.1002/esp.4857, 2020.
- 1014 Llana, M., Carreras, S., Bernatek-Jakiel, A., Ollero, A., and Nadal-Romero, E.: Agricultural
1015 land abandonment linked to pipe collapse and gully development: Reconstruction from

1016 archival SfM and LiDAR datasets, *Geoderma*, 449, 116995,
1017 <https://doi.org/10.1016/j.geoderma.2024.116995>, 2024.

1018 Liu, H. X. and Wang, L.: Mapping detention basins and deriving their spatial attributes from
1019 airborne LiDAR data for hydrological applications, *Hydrol Process*, 22, 2358–2369,
1020 10.1002/hyp.6834, 2008.

1021 Liu, T.S.: Loess Deposits in the Middle Reaches of the Yellow River, Science Press, Beijing,
1022 1–234, 1964. (in Chinese)

1023 Liu, T.S.: Loess Deposits in China, Science Press, Beijing, 1–244, 1965. (in Chinese)

1024 Panno, S. V. and Luman, D. E.: Mapping palimpsest karst features on the Illinois sinkhole plain
1025 using historical aerial photography, *Carbonate Evaporite*, 28, 201–214, 10.1007/s13146-
1026 012-0107-4, 2013.

1027 Mokroš, M., Mikita, T., Singh, A., Tomaščík, J., Chudá, J., Wężyk, P., Kuželka, K., Surový, P.,
1028 Klimánek, M., Zieba-Kulawik, K., Bobrowski, R., and Liang, X. L.: Novel low-cost
1029 mobile mapping systems for forest inventories as terrestrial laser scanning alternatives, *Int*
1030 *J Appl Earth Obs*, 104, 102512, 10.1016/j.jag.2021.102512, 2021.

1031 Moore, I. D., Grayson, R., and Ladson, A.: Digital terrain modelling: a review of hydrological,
1032 geomorphological, and biological applications, *Hydrol Process*, 5, 3–30, 1991.

1033 Morgan, R. P. C.: Soil erosion and conservation, 3rd edition, Blackwell Publishing, the United
1034 Kingdom, 2005.

1035 Niu, Y. N.: Study on provenance of Quaternary loess in Longxi area: a case from Huining,
1036 Lanzhou University Thesis, 2023. (in Chinese)

1037 Öztürk, M. Z., Şener, M. F., Şener, M., and Şimşek, M.: Structural controls on distribution of
1038 dolines on Mount Anamas (Taurus Mountains, Turkey), *Geomorphology*, 317, 107–116,
1039 10.1016/j.geomorph.2018.05.023, 2018.

1040 Panno, S., Weibel, C. P., and Li, W.: Karst regions of Illinois, Open file series 1997-02,
1041 <http://hdl.handle.net/10111/UIUCOCA:karstregionsofil19972pann>, 1997.

1042 Peng, J. B., Sun, P., Igwe, O., and Li, X.: Loess caves, a special kind of geo-hazard on loess
1043 plateau, northwestern China, *Eng Geol*, 236, 79–88, 10.1016/j.enggeo.2017.08.012, 2018.

1044 Peng, S.S.: Pronounced changes in atmospheric circulation and dust source areas during the
1045 mid-Pleistocene implicated by the Huining loess-soil sequence from the northeastern
1046 margin of the Tibetan Plateau, China University of Geosciences (Beijing) PhD Thesis,
1047 2014. (in Chinese)

1048 Pierson, T. C.: Soil pipes and slope stability, *Q. J. Eng. Geol. Hydrogeol.*, 16, 1-11, 1983.

1049 Poesen, J.: Soil erosion in the Anthropocene: Research needs, *Earth Surf Proc Land*, 43, 64–84,
1050 10.1002/esp.4250, 2018.

1051 Rajabi, A.: Sinkhole Detection and Quantification Using LiDAR Data. Electronic Theses and
1052 Dissertations, 5776. <https://stars.library.ucf.edu/etd/5776>, 2018.

1053 Richards, K. S. and Reddy, K. R.: Critical appraisal of piping phenomena in earth dams, *B Eng*
1054 *Geol Environ*, 66, 381–402, 10.1007/s10064-007-0095-0, 2007.

1055 Sevil, J. and Gutiérrez, F.: Morphometry and evolution of sinkholes on the western shore of the
1056 Dead Sea. Implications for susceptibility assessment, *Geomorphology*, 434, 108732,
1057 10.1016/j.geomorph.2023.108732, 2023.

1058 Sidle, R. C. and Bogaard, T. A.: Dynamic earth system and ecological controls of rainfall-
1059 initiated landslides, *Earth-Sci Rev*, 159, 275–291, 10.1016/j.earscirev.2016.05.013, 2016.

1060 Uchida, T., Kosugi, K., and Mizuyama, T.: Effects of pipeflow on hydrological process and its
1061 relation to landslide: a review of pipeflow studies in forested headwater catchments,
1062 *Hydrol Process*, 15, 2151–2174, DOI 10.1002/hyp.281, 2001.

1063 Vajedian, S. and Motagh, M.: Extracting sinkhole features from time-series of TerraSAR-
1064 X/TanDEM-X data, *ISPRS-J Photogramm Remote Sens*, 150, 274–284,
1065 10.1016/j.isprsjprs.2019.02.016, 2019.

1066 Vennari, C. and Parise, M.: A Chronological Database about Natural and Anthropogenic
1067 Sinkholes in Italy, *Geosciences*, 12, 200, 10.3390/geosciences12050200, 2022.

1068 Verachtert, E., Van den Eeckhaut, M., Poesen, J., and Deckers, J.: Factors controlling the spatial
1069 distribution of soil piping erosion on loess-derived soils: A case study from central
1070 Belgium, *Geomorphology*, 118, 339–348, 10.1016/j.geomorph.2010.02.001, 2010.

1071 Wang, X. G., Hu, S., Lian, B. Q., Wang, J. D., Zhan, H. B., Wang, D. Z., Liu, K., Luo, L., and

1072 Gu, C. Y.: Formation mechanism of a disaster chain in Loess Plateau: A case study of the
1073 Pucheng County disaster chain on August 10, 2023, in Shaanxi Province, China, *Eng Geol*,
1074 331, 107463, 10.1016/j.enggeo.2024.107463, 2024.

1075 Wu, Q. S., Deng, C. B., and Chen, Z. Q.: Automated delineation of karst sinkholes from LiDAR-
1076 derived digital elevation models, *Geomorphology*, 266, 1–10,
1077 10.1016/j.geomorph.2016.05.006, 2016.

1078 Yang, S. and Ding, Z.: Spatial changes in grain size of loess deposits in the Chinese Loess
1079 Plateau and implications for palaeoenvironment, *Quaternary Sciences*, 37, 934–944, 2017.
1080 (in Chinese)

1081 Yuan, Z. L., Ban, X. J., Han, F. Y., Zhang, X. Q., Yin, S. H., and Wang, Y. M.: Integrated three-
1082 dimensional visualization and soft-sensing system for underground paste backfilling, *Tunn*
1083 *Undergr Sp Tech*, 127, 104578, 10.1016/j.tust.2022.104578, 2022.

1084 Zhang, W. M., Qi, J. B., Wan, P., Wang, H. T., Xie, D. H., Wang, X. Y., and Yan, G. J.: An Easy-
1085 to-Use Airborne LiDAR Data Filtering Method Based on Cloth Simulation, *Remote Sens*,
1086 8, 501, 10.3390/rs8060501, 2016.

1087 Zhu, J. F., Nolte, A. M., Jacobs, N., and Ye, M.: Using machine learning to identify karst
1088 sinkholes from LiDAR-derived topographic depressions in the Bluegrass Region of
1089 Kentucky, *J Hydrol*, 588, 125049, 10.1016/j.jhydrol.2020.125049, 2020.

1090 Zhu, J. F. and Pierskalla, W. P.: Applying a weighted random forests method to extract karst
1091 sinkholes from LiDAR data, *J Hydrol*, 533, 343–352, 10.1016/j.jhydrol.2015.12.012, 2016.

1092 Zumpano, V., Pisano, L., and Parise, M.: An integrated framework to identify and analyze karst
1093 sinkholes, *Geomorphology*, 332, 213–225, 10.1016/j.geomorph.2019.02.013, 2019.